ISA Transactions 133 (2023) 160–183

Contents lists available at ScienceDirect

ISA Transactions

journal homepage: www.elsevier.com/locate/isatrans

Research article

Adaptive fractional-order sliding-mode disturbance observer-based robust theoretical frequency controller applied to hybrid wind–diesel power system

Dipayan Guha [a,*], Provas Kumar Roy [b], Subrata Banerjee [c]

[a] Electrical Engineering Department, Motilal Nehru National Institute of Technology Allahabad, Prayagraj, India
[b] Electrical Engineering Department, Kalyani Govt. Engineering College, West Bengal, India
[c] Electrical Engineering Department, National Institute of Technology Durgapur, West Bengal, India

ARTICLE INFO

Article history:
Received 29 August 2021
Received in revised form 17 June 2022
Accepted 24 June 2022
Available online 30 June 2022

Keywords:
Load frequency control
State observer
Fractional-order controller
Sliding-mode disturbance observer
Second-order sliding mode controller
Estimation
Robustness

ABSTRACT

This work presents design and theoretical analysis of an adaptive fractional-order sliding-mode disturbance observer (FO-SM-DOB)-aided fractional-order robust controller for frequency regulation of a hybrid wind–diesel based power system, considering endogenous/exogenous system disturbances. Adaptive FO-SM-DOB is designed to estimate unknown/uncertain lumped system disturbances, including parametric uncertainty and exogenous disturbances. Afterwards, an improved fractional-order sliding mode controller (FOSMC) augmented with the estimated output of FO-SM-DOB is designed and applied to accelerate system dynamics with minimum chattering in the control effort. The Mittag-Leffler stability theorem affirms the finite-time convergence of disturbance estimation error. Moreover, the closed-loop asymptotic stability of the overall control system has been guaranteed by applying Lyapunov argument. The effectiveness of the suggested resilient fractional-order nonlinear frequency controller is theoretically validated by performing an extensive comparative study with SMC, FOSMC (without DOB), state observer-based SMC (SOB-SMC), second-order SMC (without DOB), and conventional integer/fractional-order controllers. Simulation results establish the supremacy of the proposed resilient fractional-order nonlinear frequency controller over its other counterparts concerning fast disturbance rejection, weaker chattering, and a high degree of robustness against unknown lumped system disturbances. Further, to demonstrate the practicability and validate the effectiveness of the proposed control strategy, magnetic levitation system and IEEE 39-bus New England power system are considered and successfully tested on MATLAB platform.

1. Introduction

The existing power system network is on the verge of transformation into a "smart grid power system (SGPS)" with high penetration of distributed generations (DGs) and with rapid progression of communication technologies. The growth in renewable electricity generation and increase in demand exploit the need for SGPS in the present scenario. Among the available renewable energy resources (RERs), wind and solar photovoltaic (PV) have been extensively used in SGPS to meet the growing load demand. However, intermittence in output power and low inertia of inverter-based RERs causes undesired system oscillations, especially in the islanded mode of operation. If these oscillations persist for an extended period, the system may undergo instability. Thus, to ensure the reliable and stable operation of SGPS, the design and implementation of robust control systems are in high demand. The applied control system must be competent to handle system uncertainties, unmodelled dynamics, and exogenous disturbances in real-time operation. Furthermore, to increase the system inertia and damping of oscillations, backup energy systems (*e.g.*, diesel engine generators) run parallel to these RERs. This cooperative operation may give clean, environment-friendly sustainable power to the isolated/grid-connected loads [1,2].

Hitherto, different control techniques have been discussed in the literature for acquiring desired performance of power systems with/without RERs integrated. The literature review reveals that conventional controllers (PI/PID) are extensively applied for frequency regulation of power systems in the wake of load variation and/or RERs transients [3–7]. Conventional controllers with two/three degrees of freedom have been used to reject system disturbances quickly [8–10]. Furthermore, the performance of classical controllers in multi-loop configuration is also studied for power–frequency regulation [11,12]. The works referred to

* Corresponding author.
E-mail address: dipayan@mnnit.ac.in (D. Guha).

https://doi.org/10.1016/j.isatra.2022.06.030
0019-0578/

Nomenclature

DEG	Diesel engine generator
DOB	Disturbance observer
IO-DOB	Integer-order DOB
FO-DOB	Fractional-order DOB
FO-SM-DOB	Fractional-order sliding-mode DOB
FOSMC	Fractional-order sliding mode controller
hy-WD-PS	Hybrid wind–diesel based power system
MagLev	Magnetic levitation
ODE	Ordinary differential equation
PV	Photovoltaic
RERs	Renewable energy resources
PID	Proportional–integral–derivative
SOB-SMC	State observer-based SMC
SGPS	Smart grid power system
SM	Sliding mode
SOSMC	Second-order SMC
WPG	Wind turbine generator
P_w	Electrical power output of WPG (pu)
P_m	Mechanical power output of WPG (pu)
P_L	Load demand (pu)
H_w	Wind system Inertia constant (s)
H_D	Diesel system Inertia constant (s)
λ	Tip speed ratio of WT
β	Blade pitch angle of WT
k_{fc}	Fuel coupling constant (pu kW/Hz)
K_D	Integral gain of governor controller of DEG (pu kW/Hz)
T_1	Time constant of DEG (s)
K_{pc}	Gains of WT's blade characteristic
V_w	Wind velocity (m/s)
R_{blade}	Radius of the WT's blade (m)
T_{hp1}&T_{hp2}	Time constant of hydraulic actuator of WT (s)
K_{ph2}&K_{ph3}	Gains of hydraulic actuator of WT
$\Delta\omega_1$&$\Delta\omega_2$	Frequency deviation in WPG and DEG units (Hz), respectively

above consider linear controllers whose performance is deteriorated with modelling error, unmodelled dynamics, parameter uncertainty, and exogenous disturbances.

In recent years, fractional-order (FO) calculus has gained considerable research impetus to describe the non-local behaviour of dynamical systems more accurately with memory and hereditary properties than the ordinary differential equation (ODE)-based approach. Different ways of describing fractional derivatives and integrals include Riemann–Liouville (RL), Caputo, Marchaud, Hilfer, Atangana–Baleanu, etc. [13]. However, Caputo fractional derivative has been one of the most applied operators to describe dynamical systems due to:

(i) The Caputo fractional derivative of constant is zero.
(ii) Unlike RL fractional derivative, Caputo derivative does not require to mention fractional initial value. Caputo derivative requires a more natural initialization of initial conditions when used for fractional differential equations (same as integer-order differential equations).

The extensive literature review reveals that integrating FO calculus with integer-order (IO) controllers increases design flexibility and controller degree-of-freedom (additional tuning parameters), resulting in better system outputs. Guha et al. demonstrated the efficacy of an FO-controller in cascaded configuration to attenuate power–frequency oscillations of a hybrid power system [14]. FO-fuzzy aided classical controller is applied for frequency control of islanded microgrids [15]. Arya [16] developed cascade fuzzy-aided FO-controllers for frequency regulation of a power system. Frequency control of power systems employing an optimized fuzzy-aided hybrid controller is presented in [17]. These FO controllers show substantial improvement in the system performance at a given operating condition. The linear controllers (PID or its variant) have been utilized in [14–17] for frequency regulation of power systems. Its performance deteriorates with unmodelled system dynamics, parametric uncertainty, external disturbances, etc. Moreover, the design of fuzzy-based controllers requires optimum selections of input parameters, such as rule base, membership function, defuzzification rule, scaling factors, etc. Hence, the design of a resilient frequency controller is imperative to maintain the synchronism between the power generation and load demand for the stable operation of the hybrid power system.

Sliding mode controller (SMC) has been extensively used in control engineering practices because of its computational simplicity, high robustness against exogenous disturbances, invariability to uncertain parameters, and fast global state convergence [18,19]. The performance of ant lion optimized hybrid intelligent PID-based SMC has been investigated for frequency regulation of interconnected multi-area power systems [20]. However, chattering at the SMC's output is caused due to parasitic unmodelled dynamics and finite-frequency switching gain that limits its practical implementation. Moreover, the conventional SMC is sensitive to mismatched plant disturbances. To alleviate chattering with a high degree of robustness, continuous effort in SMC design has been noticed, *e.g.*, boundary layer approach, FO-aided SMC, fuzzy-based SMC, etc. [21–23]. The FO calculus adds memory to the SMC design, reducing chattering in the control input. An FO-SMC is designed and applied to study the stability of a multimachine power system. Improvement in chattering at the controller output with FO calculus has been shown over SMC [24]. Bagheri et al. [25] have studied the frequency regulation problem of islanded microgrid systems employing terminal SMC (TSMC) by choosing a nonlinear FO-type sliding surface. Presented results show improvement in frequency damping subjected to large load/generation disturbances. In the design of the controller, only exogenous disturbances have been considered. Moreover, the state convergence in TSMC is slower than in linear SMC. The proper estimation of the boundary value of disturbance gradient is required to design TSMC, which is difficult to estimate in practice. An adaptive integral higher-order SMC is designed for load frequency control of an interconnected power system [26]. Adaption law is also introduced to estimate the unknown bound of system uncertainties. However, during exigency conditions (*i.e.,* high penetration level of inverter-based renewable), inaccurate disturbance estimation may degrade the performance of power systems. Furthermore, unmodelled dynamics were not considered while designing the controller [26]. In the above-mentioned references, it is assumed that system disturbances are available for measurement.

Disturbance observer (DOB)-based SMC is investigated in [27,28], and presented results show improved controller performance concerning weaker chattering in control law. In [29], a disturbance observer (DOB) is studied to estimate uncertain system disturbances with a reduced-order state observer. Subsequently, the estimation is utilized as an activating signal to cancel the effect of the same disturbance through the feedback control approach. An extended state observer-based FO-SMC is designed and applied to minimize the frequency deviation by controlling

the governor of generation units [30]. In this work, the linearized approximated wind generation plant is undertaken to study the controller performance. However, the feasibility of DOB relies on measuring disturbances, which is impractical. Besides the works mentioned above, the effectiveness of FO-SMC has been well-studied in other control problems [31–34].

Recently, the sliding-mode (SM) approach has been introduced in the design of DOB called sliding-mode DOB (SM-DOB) to alleviate chattering and fast active compensation of external disturbances on the system performance. Mathematical models of disturbance are not required explicitly for the realization of SM-DOB, making it more effective in reducing chattering [35]. Moreover, designing a DOB based on SM-theory increases robustness and provide feed-forward compensation to plant disturbances. The effectiveness of SM-DOB based control systems has been shown in different control engineering problems, such as twin rotor MIMO system [36], missile control application [37], optical disc drives [38], fault-tolerant control of power system [39], etc. However, SO-DOB suffers from shortcomings [38], such as (i) due to unknown bound on estimation error, conservative switching gain in the design yields limited alleviation of chattering, and (ii) it provides non-zero estimation error at steady-state for time-varying disturbances. Besides these, higher-order SMC [40,41], adaptive SMC [42], terminal SMC [43], neural network-based SMC [44], etc., have been researched to minimize the chattering and improve the nominal performance of different control engineering problems.

Since FO theory describes the plant dynamics more accurately than ODE models [19], the demand for developing FO-based robust control systems to cope with plant mismatches is increased significantly. For the FO-type dynamical systems, the integer-order DOB cannot give any information about the FO derivative of plant disturbances except its estimation. Moreover, the introduction of FO calculus makes DOB flexible and increases the controller degree-of-freedom for fast active compensation of unknown system disturbances. Furthermore, it allows more flexibility in selecting the order, relative degree, and bandwidth of the disturbance observer filter (*i.e.*, Q-filter). This work has attempted to develop a theoretical adaptive FO-aided SM-DOB (FO-SM-DOB) for the active compensation of lumped plant disturbances, including parametric uncertainty and exogenous disturbances. Subsequently, this disturbance estimation is utilized to cancel out the plant disturbances effect through the proposed feedback control mechanism (*i.e.,* FOSMC). The advantages of FO-SM-DOB for estimating plant lumped uncertainties are discussed as follows:

(i) It increases degree-of-freedom in the design and results in better disturbance rejection ability of the closed-loop control system during system contingency. Furthermore, FO-calculus augmentation has significantly increased the speed of asymptotic convergence of estimation error.
(ii) The resilience of the closed-loop control system has been significantly improved by choosing the sliding mode (SM) strategy, which effectively compensates matched and unmatched system uncertainties.
Since the lumped plant disturbance is precisely estimated employing an adaptive FO-SM-DOB, the magnitude of estimation error can be kept small compared to the actual disturbance signal, resulting in a smaller switching gain of the discontinuous control law. Furthermore, SM-aided DOB does not require mathematical models of system disturbances, resulting in design flexibility.
(iii) The SM-type strategy offers feed-forward compensation to plant disturbances, resulting in fast damping of undue system oscillations caused by uncertain/unknown plant disturbances.

To the best of the author's knowledge in the references mentioned above, the frequency regulation problem of a power system having RERs integrated has not been studied by applying/designing adaptive SM-FO-DO based FOSMC, considering system uncertainty and exogenous disturbances. Given the preceding discussion, the following attributes encourage authors to perform the current study:

(i) Designing resilient nonlinear frequency controllers for the low-inertia intermittent inverter-based highly nonlinear/linearized hybrid power systems is highly demanded to maintain a reliable and stable power supply to customers.
(ii) DOB has been identified as an alternative to feed-forward compensator to effectively countermeasure unknown/uncertain lumped plant disturbances. However, in the design of DOB, the mathematical model of the disturbance must be known. On the other hand, developing a sliding mode control law is straightforward and does not explicitly require the mathematical model of the disturbance.
(iii) SMC has been extensively used as a frequency regulator because of its high robustness. However, chattering at the SMC's output is a key concern for designers. Moreover, fast asymptotic state convergence to the defined sliding surface is highly demanded. Thus, the design of refined control effort to acquire the above-said objectives is imperative.
(iv) The extensive review of the available state-of-art reveals that FO calculus has been extensively used to describe the supplementary controllers for frequency regulation against unknown system disturbances. The key advantage is that it makes the design less conservative or aggressive by introducing extra tuning parameters.

The significant contributions in the present work are summarized as follows:

(i) An adaptive FO-SM-DOB is designed to estimate lumped plant disturbances. An adaptive law has been introduced in the developed FO-type SM-DOB that increases the degree of robustness of the closed-loop control system against unmodelled dynamics, parametric uncertainty, and exogenous disturbances.
(ii) A resilient FO-sliding mode (FOSMC) feedback control law is designed by augmenting the lumped disturbance estimation to cope with unknown/uncertain system uncertainties.
(iii) A hybrid wind–diesel power system (hy-WD-PS) is undertaken to perform the analysis, considering diverse operating scenarios. The detailed state–space model of the hy-WD-PS has been obtained to perform the simulation studies.
(iv) The design parameters of the proposed resilient fractional-order nonlinear controller are obtained using the pole placement approach.
(v) The finite-time convergence of estimation error and asymptotic closed-loop stability of the developed control system have been affirmed using the Mittag-Leffler stability theorem and the Lyapunov argument.
(vi) The effectiveness of the proposed fractional-order robust controller has been theoretically validated by performing a comparative study with conventional IO/FO controllers, IO/FO SMC, state observer-based SMC (SOB-SMC), and second-order SMC (without DOB).
(vii) Finally, to demonstrate the efficacy of the proposed resilient fractional-order nonlinear controller, the dynamic stability of magnetic levitation system and IEEE 39-bus New England large power system has been inspected and successfully tested on MATLAB platform.

The remaining part of the paper is arranged as follows: Section 2 presents the small-signal stability model (state space) of the undertaken hybrid power system (hy-PS). The proposed control methodology applied for frequency regulation of hy-PS is discussed in Section 3. In Section 4, the performance of the proposed controller has been theoretically validated through extensive comparative studies, considering different operating environments. Finally, the concluding remarks of the present work with future scopes are provided in Section 5.

2. System modelling

This paper attempts to theoretically study the small-signal stability problem of a hybrid wind–diesel power system (hy-WD-PS) subjected to small-size of system disturbances. To carry out the investigation, a linearized approximated mathematical model of the test system is considered. Fig. 1 shows the pole-zero model of hy-WD-PS, which comprises a wind energy conversion system (WECS) operating parallel with a diesel engine generator (DEG) [1,2]. The rated parameters of the studied test system are taken from [1,2] and presented in Appendix A. The dynamical model of the undertaken hy-WD-PS, considering unknown exogenous disturbances and parameter uncertainty, can be expressed in state–space as

$$\begin{cases} \dot{x}(t) = (A + \Delta A)\, x(t) + (B + \Delta B)\, u(t) + B_d d(t) \\ y(t) = Cx(t) \end{cases} \tag{1}$$

Assuming $\xi(t) = [\Delta A x(t) + \Delta B u(t) + B_d d(t)]$, Eq. (1) can be simplified as

$$\begin{cases} \dot{x}(t) = Ax(t) + Bu(t) + \xi(t) \\ y(t) = Cx(t) \end{cases} \tag{2}$$

where $x(t) \in \mathbb{R}^n$ is the state vector; A, B, and C are state, input, and output matrices with appropriate dimension, respectively; B_d defines the disturbance matrix; $y(t)$ is the output variable; $d(t) \in \mathbb{R}^n$ defines exogenous plant disturbance; $u(t) \in \mathbb{R}^n$ is the control effort; ΔA, ΔB are the variation of state and input matrices due to parametric uncertainty, respectively; $\xi(t)$ defines the lumped plant disturbance. With extensive penetration of inverter-based renewable resources and dynamic changes in environmental conditions, the operating point may be perturbed in the vicinity of nominal operating conditions. Hence, it is imperative to design a frequency controller which is highly insensitive to these perturbations. The literature review reveals that authors have primarily analysed the system performance considering ±20% or ±25% variation in system parameters from nominal conditions [45–47]. Thus, referring to the works reported in [45,46], ±25% dynamic variation in system parameters from the nominal settings has been considered to assess the performance of the proposed control methodology. Since the variation of operating points against small-size of disturbance is always about the vicinity of nominal conditions under the small-signal stability framework; therefore, it is convenient to design the controller with ±25% variation in system parameters. Moreover, the sensitivity of the developed controller is further evaluated for other parametric uncertainty levels in the results section.

Assumption 1. The boundedness of ΔA and ΔB are assumed ±25% from nominal settings to obtain the dynamical model of undertaken hy-WD-PS.

The adopted WECS comprises wind aerodynamics, a mechanical coupling shaft with gearbox, and an induction generator. The wake effect is the aggregated impacts of adjacent wind turbines (WTs) on each other. Due to this effect, wind speed is reduced, and subsequently, the output power of a wind farm is also reduced [48]. To quantify the mastery of the proposed adaptive FO-SM-DOB aided FOSMC to handle system uncertainties, wake effects in WTs have been considered in the wind aerodynamic model. The mechanical power output (P_m) with wake effect in WTs can be obtained using Eq. (3) [48].

$$P_m = \frac{1}{2}\rho A_T C_p(\lambda, \beta) V_{wake}^3 \tag{3}$$

$$\text{where} \begin{cases} V_{wake} = V_w \left[1 - \sum_{i=1}^{n} \left(1 - \sqrt{1 - \left(\frac{F_T}{\rho \pi r^2 V_w^2}\right)}\right) \left(\frac{r}{(r + k\Delta x)}\right)^2\right] \\ C_p(\lambda, \beta) = C_1 \left(\frac{C_2}{\lambda_I} - C_3\beta - C_4\right) e^{-\frac{C_5}{\lambda_I}} + C_6\lambda_T \\ \frac{1}{\lambda_I} = \frac{1}{\lambda + 0.08\beta} - \frac{0.035}{\beta^3 + 1};\ \ \lambda_T = \frac{\omega_r r}{V_w};\ \ A_T = \frac{\pi d^2}{4} \end{cases}$$

where ρ is air density $\left(\text{kg/m}^3\right)$; d is the diameter of WT's rotor (m); C_p is power coefficient; λ_T is optimal tip-speed ratio (TSR); λ_I is intermittent TSR; β represents blade pitch angle; F_T is thrust force; k is a decreasing coefficient ($k = 0.05$ for offshore WT and $k = 0.075$ for onshore WT); Δx is the distance between two consecutive WTs; V_w is effective wind velocity (m/s).

The mechanical coupling shaft of WECS has been represented by a two-mass model, as given in [48,49]. The differential equation model of mechanical coupling shaft with gear train can be expressed as

$$\begin{cases} \dot{\omega}_{WT} = -\left(\frac{D_{WT} + D_{shaft}}{J_{WT}}\right)\omega_{r,WT} + \left(\frac{D_{shaft}}{J_{WT}}\right)\omega_{gen} \\ \qquad\qquad - \left(\frac{1}{J_{WT}}\right)T_{\text{int}} + \left(\frac{1}{J_{WT}}\right)d(t) \\ \dot{\omega}_{gen} = \left(\frac{D_{shaft}}{2J_{gen}}\right)\omega_{r,WT} - \left(\frac{D_{gen} + D_{shaft}}{J_{gen}}\right)\omega_{gen} \\ \qquad\qquad + \left(\frac{1}{n_{gear}J_{gen}}\right)T_{\text{int}} - \left(\frac{1}{J_{gen}}\right)u(t) \\ \dot{T}_{\text{int}} = K_{shaft}\left(\omega_{WT} - \frac{\omega_{gen}}{n_{gear}}\right) \end{cases} \tag{4}$$

where ω_{WT}, ω_g are the angular speed of rotor of WTs and generator, respectively; J_{WT}, J_{gen} are the moment of inertia of rotor of WTs and generator, respectively; D_{WT}, D_{gen}, and D_{shaft} are the damping constant of WT, generator, and coupling shaft, respectively; n_{gear} is gear turns ratio; T_{int} is the shaft internal torque.

Assuming an ideal/lossless generator, the output power (P_w) of the generator can be obtained using Eq. (5) [49]. As the generated torque $\left(T_{gen}\right)$ cannot be controlled instantaneously, the dynamic model of the generator is represented by a first-order time-lag model, as given in Eq. (6) [49].

$$P_w = T_{gen}\omega_g \tag{5}$$

$$\frac{dT_{gen}}{dt} = \left(-\frac{1}{\tau_{gen}}\right)T_{gen} + \left(\frac{1}{\tau_{gen}}\right)T_{control} \tag{6}$$

where τ_{gen} is the generator time constant; $T_{control}$ defines the control torque that regulate the output power of WPG against uncertain wind speed. The state, input, and disturbance matrices of the test system considering the state variables marked in Fig. 1 are computed and provided in Appendix B.

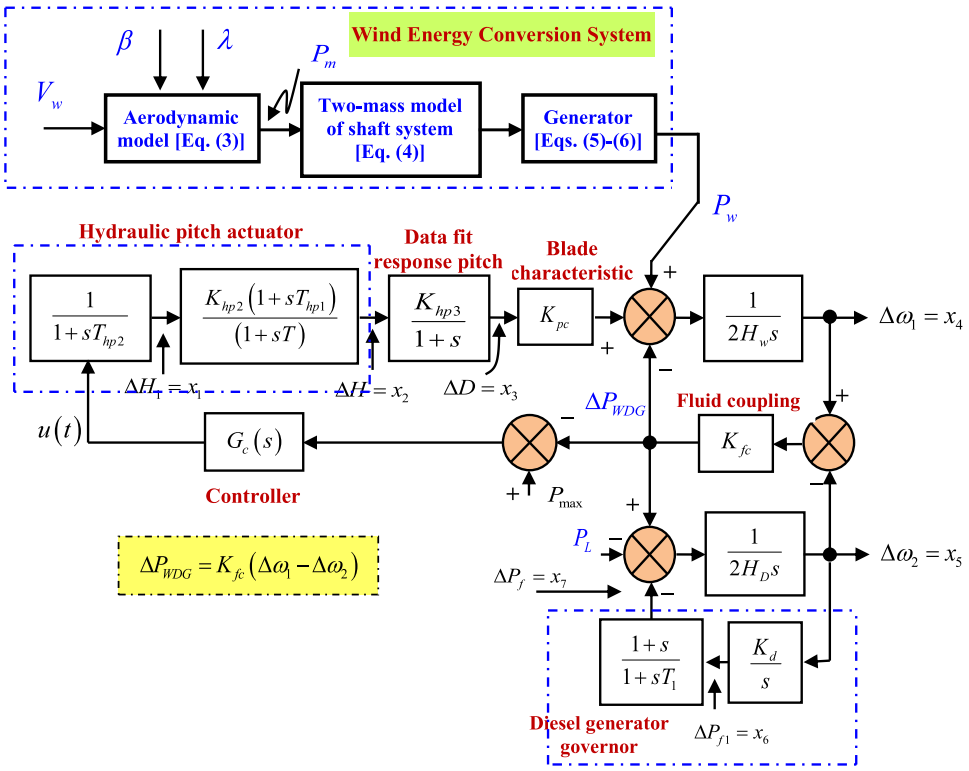

Fig. 1. Small-signal stability model of hy-WD-PS.

3. Control methodology

The main objective of the present work is to design a resilient fractional-order nonlinear frequency controller to achieve desired system output following system disturbances. Initially, an adaptive fractional-order sliding-mode disturbance observer (FO-SM-DOB) is designed to estimate lumped plant disturbances ($\xi(t)$), including parametric uncertainty and exogenous disturbances. Subsequently, an improved FOSMC is realized by augmenting the estimation for fast disturbance rejection and better system stability. This section presents a brief theory of IO-DOB/FO-DOB following the mathematical model of the proposed adaptive FO-SM-DOB aided FOSMC.

3.1. Integer-order/fractional-order disturbance observer

Physical plants often experience external disturbances that may cause deviation of output from desired value (steady-state inaccuracy); the large size of disturbances even may cause instability. Hence, an effective control strategy must be realized and applied to handle these unpredictable disturbances and maintain system stability. Disturbance observer (DOB) estimates fast variation of unknown/uncertain system disturbances, and the estimate is used as an activating/compensating signal to cancel the effects of the same disturbances. Fig. 2 illustrates a closed-loop control system with an integer-order DOB (IO-DOB).

From Fig. 2, the output of IO-DOB can be computed as [19]

$$Y(s) = \frac{G_p(s)\,G_n(s)}{G_n(s) + \left[G_p(s) - G_n(s)\right]Q(s)}C(s) + \frac{G_p(s)\,G_n(s)\,[1 - Q(s)]}{G_n(s) + \left[G_p(s) - G_n(s)\right]Q(s)}D(s) \quad (7)$$

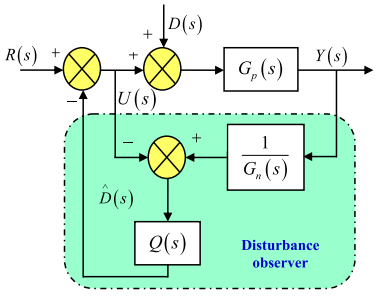

Fig. 2. Model of frequency-domain integer-order disturbance observer (IO-DOB).

where $G_p(s)$ is the plant model; $G_n(s)$ is nominal model of the plant; $C(s)$, $Y(s)$, and $D(s)$ are the controlled output, measured signal, and external disturbance, respectively; $\hat{D}(s)$ is the estimation of disturbance. It is apparent from Eq. (7) that the disturbance compensation ability of DOB is susceptible to order, relative degree, and bandwidth of the disturbance filter or Q-filter. Based on the following two cases, Q-filter can be realized [19].

(i) $Q(s) \to 1$

$$\frac{G_p(s)\,G_n(s)}{G_n(s) + \left[G_p(s) - G_n(s)\right]Q(s)} \to G_n(s) \text{ and}$$
$$\frac{G_p(s)\,G_n(s)\,[1 - Q(s)]}{G_n(s) + \left[G_p(s) - G_n(s)\right]Q(s)} \to 0$$

Dynamic features of the system are similar to nominal model of the plant.

(ii) $Q(s) \to 0$

$$\frac{G_p(s)G_n(s)}{G_n(s)+\left[G_p(s)-G_n(s)\right]Q(s)} \to G_p(s) \text{ and}$$
$$\frac{G_p(s)G_n(s)\left[1-Q(s)\right]}{G_n(s)+\left[G_p(s)-G_n(s)\right]Q(s)} \to G_p(s)$$

The system can be approximated as an open-loop system.

Considering the above two cases, *Q-filter* is typically designed as a low-pass filter such that estimated disturbance equals actual plat disturbance at low frequency. As mentioned before, the performance of DOB depends on the order, relative degree and bandwidth of the Q-filter; hence, the disturbance compensation ability of DOB can be improved by making the design of Q-filter less conservative or aggressive. Moreover, the FO calculus describes the dynamical system accurately; for them, satisfactory system performance cannot be achieved by employing IO-DOB. The introduction of FO calculus makes DOB flexible and increases the controller's degree-of-freedom for fast active compensation of unknown system disturbances. Furthermore, it allows more flexibility in selecting the order, relative degree, and bandwidth of Q-filter. Unlike IO-DOB [Fig. 2], the order of the Q-filter is a real positive number in FO-DOB, as defined in Eq. (8).

$$Q(s) = \left(\frac{1}{\tau_{filter}s+1}\right)^{\delta} \quad \because \delta \in \mathbb{R} \tag{8}$$

where τ_{filter} is the time constant of Q-filter; δ is the fractional power of Q-filter. Based on broken-line approximation, Eq. (8) can be simplified in the frequency range $[\omega_l, \omega_h]$ as [19]

$$G_\delta(s) = \left[\frac{1+{}^{s}/_{\omega_h}}{1+{}^{s}/_{\omega_l}}\right]^{\delta} \tag{9}$$

where $\omega_l = \frac{1}{\tau_{filter}}$; $\omega_h = 10^4$. Eq. (9) can be approximated as cascading rational functions defined in Eqs. (10)–(11).

$$\begin{cases} G_N(s) = \prod_{i=0}^{N-1} \frac{1+{}^{s}/_{\omega_i^*}}{1+{}^{s}/_{\omega_i}} \\ G_\delta(s) = \lim_{N\to\infty} G_N(s) \end{cases} \tag{10}$$

$$\text{where } \begin{cases} \omega_i = \omega_l \left(\frac{\omega_h}{\omega_l}\right)^{\left(i-\frac{1}{2}-\frac{\delta}{2}\right)/N} \\ \omega_i^* = \omega_l \left(\frac{\omega_h}{\omega_l}\right)^{\left(i+\frac{1}{2}+\frac{\delta}{2}\right)/N} \end{cases} \tag{11}$$

In this work, Caputo fractional derivative has been chosen for developing the computational model of the proposed resilient fractional-order nonlinear controller due to the advantages mentioned in the Introduction Section.

Assumption 2 ([19]). The lumped plant disturbance $\xi(t)$ is upper bounded, *i.e.*, $|\xi(t)| \le \eta$, where η is an unknown positive constant.

Lemma 1 ([19]). *Let, $p(t) \in \mathbb{R}$ be a continuously differentiable function. For any time instant $t_1 \ge 0$ and $\beta \in (0, 1]$, the following relationship is hold*

$$\frac{1}{2}D^{\beta}p^2(t) \le p(t)D^{\beta}p(t) \tag{12}$$

β defines the fractional power.

Theorem 1 ([19]). *Let, the dynamics of a FO-autonomous system be*

$$D^{\beta}x(t) = f(x(t)) \qquad \forall\beta \in (0, 1] \tag{13}$$

Let $x(t) = 0$ be the equilibrium point of the system Eq. (13).

If, $x(t)f(x(t)) \le 0 \quad \forall x(t)$

then, the origin of Eq. (13) is stable.

If, $x(t)f(x(t)) < 0 \quad \forall x(t) \ne 0$

then, the origin of Eq. (13) is asymptotically stable. This theorem is known as "Mittag-Leffler stability" applied to FO systems (FO version of Lyapunov stability theorem).

3.2. Adaptive fractional-order sliding-mode disturbance observer (FO-SM-DOB)

In this section, the computational model of the proposed adaptive FO-SM-DOB is designed considering a FO system. However, the same design approach can be extended to IO systems. Let the dynamical model of a FO system be

$$\begin{cases} D^{\beta}x(t) = f(x(t)) + u(t) + \xi(t) \\ \text{where } \beta \in (0, 1] \end{cases} \tag{14}$$

where $f(.)$ is the nonlinear function. Let the dynamical model of FO-SM-DOB, for the system defined in Eq. (14), is realized as

$$\sigma(t) = x(t) - p(t) \tag{15}$$
$$D^{\beta}p(t) = u(t) - \chi(t) \tag{16}$$
$$\chi(t) = -\kappa_0 \text{sgn}(\sigma(t)) - \hat{\eta}\text{sgn}(\sigma(t)) - |f(x(t))|\,\text{sgn}(\sigma(t)) \tag{17}$$
$$\hat{\xi}(t) = -\chi(t) - f(x(t)) \tag{18}$$

where $\sigma(t)$ is the sliding surface; $p(t)$ and $\chi(t)$ are the state variables of FO-SM-DOB; $\hat{\xi}(t)$ is the estimation of $\xi(t)$; $\hat{\eta}$ is the estimation of disturbance upper bound η; $\kappa_0 (> 0)$ is the design parameter of FO-SM-DOB. Taking βth derivative of sliding surface defined in Eq. (15), we get

$$D^{\beta}\sigma(t) = D^{\beta}x(t) - D^{\beta}p(t) \tag{19}$$

Solving Eqs. (14), (16), and (19), we get

$$\begin{cases} D^{\beta}\sigma(t) = [f(x(t)) + u(t) + \xi(t)] - [u(t) - \chi(t)] \\ \Rightarrow D^{\beta}\sigma(t) = f(x(t)) + \xi(t) + \chi(t) \end{cases} \tag{20}$$

3.2.1. Asymptotic stability analysis of the developed adaptive FO-SM-DOB

Let the Lyapunov candidate be

$$V_1(\sigma, \tilde{\eta}) = \frac{1}{2}\sigma^2 + \frac{1}{2\kappa_1}\tilde{\eta}^2 \tag{21}$$

where $\kappa_1 (> 0)$ is the design parameter; $\tilde{\eta}\left[= \left(\eta - \hat{\eta}\right)\right]$ is estimation error. Using Lemma 1, the βth derivative of Eq. (21) is computed as

$$D^{\beta}V_1 \le \sigma D^{\beta}\sigma + \frac{1}{\kappa_1}\left(\eta - \hat{\eta}\right)D^{\beta}\left(\eta - \hat{\eta}\right) \tag{22}$$

According to Caputo derivative definition, FO derivative of a constant is zero. Hence, Eq. (22) is simplified as

$$D^{\beta}V_1 \le \sigma D^{\beta}\sigma - \frac{1}{\kappa_1}\left(\eta - \hat{\eta}\right)D^{\beta}\hat{\eta} \tag{23}$$

Solving Eqs. (20) and (23), we get

$$D^{\beta}V_1 \leq \sigma\left[f\left(x\left(t\right)\right)+\xi\left(t\right)+\chi\left(t\right)\right]-\frac{1}{\kappa_1}\left(\eta-\hat{\eta}\right)D^{\beta}\hat{\eta} \tag{24}$$

Considering Assumption 2, Eq. (24) can be re-written as

$$D^{\beta}V_1 \leq |\sigma|\,\eta+|\sigma|\,|f\left(x\left(t\right)\right)|+\sigma\chi\left(t\right)-\frac{1}{\kappa_1}\left(\eta-\hat{\eta}\right)D^{\beta}\hat{\eta} \tag{25}$$

The adaptive law for $\hat{\eta}$ is defined as

$$D^{\beta}\hat{\eta}=\kappa_1\,|\sigma| \tag{26}$$

Solving Eqs. (17), (25), and (26), we get

$$\begin{cases} D^{\beta}V_1 \leq |\sigma|\,\eta+|\sigma|\,|f\left(x\right)| \\ +\sigma\left(-\kappa_0\mathrm{sgn}\left(\sigma\right)-\hat{\eta}\mathrm{sgn}\left(\sigma\right)-|f\left(x\right)|\,\mathrm{sgn}\left(\sigma\right)\right) \\ -\frac{1}{\kappa_1}\left(\eta-\hat{\eta}\right)\kappa_1\,|\sigma| \\ \Rightarrow D^{\beta}V_1 \leq |\sigma|\,\eta+|\sigma|\,|f\left(x\right)|-\kappa_0\,|\sigma|-\hat{\eta}\,|\sigma|-|\sigma|\,|f\left(x\right)| \\ -|\sigma|\,\eta+\hat{\eta}\,|\sigma| \end{cases}$$

$$\Rightarrow D^{\beta}V_1=-\kappa_0\,|\sigma|<0 \qquad \forall\sigma\neq 0 \tag{27}$$

From Eq. (27), it is seen that the fractional derivative of the Lyapunov candidate is negative definite for any $\kappa_0 > 0$. Thus, invoking Theorem 1, it may be concluded that the origin of the sliding surface of FO-SM-DOB is asymptotically stable. The value of switching gain κ_0 has to be set higher than the upper bound of the lumped plant disturbance (η) in order to ensure the existence of the sliding surface and finite-time asymptotic convergence of estimation error. Moreover, this is also required to handle the system performance against large-size exogenous disturbance. The design procedure of FO-SM-DOB is summarized in Theorem 2.

Theorem 2. *Defining fractional-order autonomous system Eq. (14) with unknown lumped plant disturbance $\xi\left(t\right)$, which is to be estimated employing FO-SM-DOB [Eqs. (15)–(18)]. The adaptive law of upper bound of $\xi\left(t\right)$ is to be chosen as given in Eq. (26). Thus, by proper tuning of design parameters κ_0 and κ_1, the plant disturbances can be well estimated using the proposed adaptive FO-SM-DOB.*

3.3. Fractional-order SMC (FOSMC)

In this sub-section, a fractional-order sliding mode controller (FOSMC) is designed by augmenting the estimated output of lumped system disturbances. The control objective is to design a control law $u\left(t\right)$ that drives system output asymptotically converges to equilibrium point in finite time with least steady-state error and minimum chattering in control effort. Fig. 3 depicts the block diagram of the proposed resilient fractional-order nonlinear control method. Let the sliding surface for the proposed FOSMC be

$$\sigma_c\left(x\right)=a_1x\left(t\right)+a_2D^{\alpha}x\left(t\right) \tag{28}$$

where $a_1 > 0, a_2 > 0$ are the designed parameters of SMC. The time derivative of Eq. (28) gives

$$\dot{\sigma_c}\left(x\right)=a_1\dot{x}\left(t\right)+a_2D^{1+\alpha}\dot{x}\left(t\right) \tag{29}$$

Solving Eqs. (1) and (29), we get

$$\dot{\sigma_c}\left(x\right)=a_1\dot{x}\left(t\right)+a_2D^{1+\alpha}\left(Ax\left(t\right)+Bu\left(t\right)+\xi\left(t\right)\right) \tag{30}$$

The equivalent control law $\left(u_{eq}\right)$ can be obtained by setting $\dot{\sigma_c}\left(x\right)=0$ in Eq. (30), *i.e.*,

$$\begin{cases} 0=a_1\dot{x}\left(t\right)+a_2D^{1+\alpha}\left(Ax\left(t\right)+Bu\left(t\right)+\xi\left(t\right)\right) \\ \Rightarrow u_{eq}\left(t\right)=-B^{-1}\left[\left(\frac{a_1}{a_2}\right)D^{-\alpha}x\left(t\right)+Ax\left(t\right)+\hat{\eta}\right] \end{cases} \tag{31}$$

The reaching law for the proposed FOSMC is chosen as

$$u_{rh}\left(t\right)=-B^{-1}\left(\frac{1}{a_2}D^{-1-\alpha}\left[a_3\sigma_c\left(x\right)+a_4\mathrm{sgn}\left(\sigma_c\left(x\right)\right)\right]\right) \tag{32}$$

where $a_3 > 0, a_4 > 0$ are the constant gains. The control law of FOSMC using Eqs. (31) and (32) is computed as

$$u\left(t\right)=-B^{-1}\left[\left(\frac{a_1}{a_2}\right)D^{-\alpha}x\left(t\right)+\frac{1}{a_2}D^{-1-\alpha}\times\left[a_3\sigma_c\left(x\right)+a_4\mathrm{sgn}\left(\sigma_c\left(x\right)\right)\right]+Ax\left(t\right)+\hat{\eta}\right] \tag{33}$$

It is assumed that B is invertible. If B is singular matrix, then pseudo-inverse of B can be considered to design Eq. (33). It is desired to select the appropriate value of a_1 such that $|a_1B| \neq 0$ and a_2 should be selected to ensure that the real part of eigenvalues of $|A-Ba_2|$ is negative. The pole placement approach is applied to select the gains (a_1, a_2) of SMC/FOSMC to reduce the design complexity. The desired pole locations in the *s-plane* are chosen as five times of distance of the real part of the dominant pole(s). Linear quadratic regulator (LQR) or optimization techniques can be applied to select these settings. For different values of α, the system performances have been measured in terms of speed of state convergence and chattering in control input. The optimum result corresponding to $\alpha = 0.57$ is selected to carry out the present analysis. The fractional power of FO-SM-DOB is also set by trial-and-error, *i.e.*, $\beta = 0.69$. The switching gains are to be set (based on designer experience) by making a trade-off between the "*speed of state convergence*" and "*permissible chattering at the control input*".

Remark. Saturating saturation is a key issue in a feedback control system when control effort exceeds the physical limit. Hence, to deal with this problem, it is desired to maintain the size of control signals within the physical limits of final control elements/actuators. The presented results show that the control input generated with the proposed controller [Eq. (33)] is small and will not cause actuator saturation.

Moreover, an anti-windup scheme can also be adopted and implemented to handle the saturating saturation problem in feedback control systems.

3.3.1. Asymptotic stability analysis of closed-loop control system

Let the Lyapunov candidate be

$$V_2\left(\sigma_c\left(x\right)\right)=\frac{1}{2}\sigma_c^2\left(x\right) \tag{34}$$

The time derivative of Eq. (34) gives

$$\dot{V}_2\left(\sigma_c\left(x\right)\right)=\sigma_c\left(x\right)\dot{\sigma_c}\left(x\right) \tag{35}$$

Substituting Eq. (30) into Eq. (35), we get

$$\dot{V}_2\left(\sigma_c\left(x\right)\right)=\sigma_c\left(x\right)\left[a_1\dot{x}\left(t\right)+a_2D^{1+\alpha}\left(Ax\left(t\right)+Bu\left(t\right)+\xi\left(t\right)\right)\right] \tag{36}$$

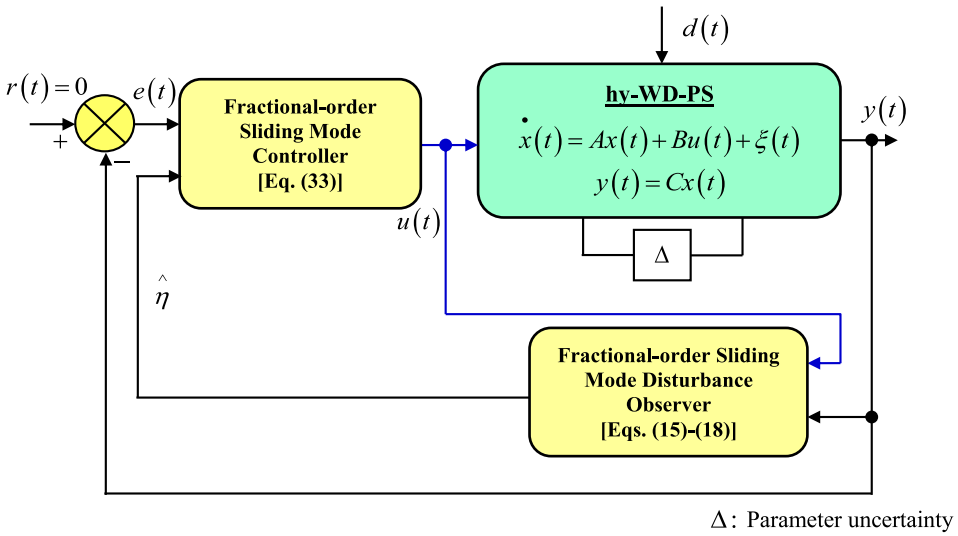

Fig. 3. Block diagram of the proposed resilient fractional-order nonlinear control method.

$$\dot{V}_2(\sigma_c(x)) = \sigma_c(x)\left[a_1\dot{x}(t) + a_2 D^{1+\alpha}\left(Ax(t) - \left[\begin{matrix}\left(\frac{a_1}{a_2}\right)D^{-\alpha}x(t) + Ax(t) + \hat{\eta} \\ +\frac{1}{a_2}D^{-1-\alpha}\begin{bmatrix}a_3\sigma_c(x) \\ +a_4\mathrm{sgn}(\sigma_c(x))\end{bmatrix}\end{matrix}\right] + \xi(t)\right)\right]$$

$$\Rightarrow \dot{V}_2(\sigma_c(x)) = \sigma_c(x)\begin{bmatrix}a_1\dot{x}(t) + a_2 D^{1+\alpha}Ax(t) - a_1\dot{x}(t) - a_2 D^{1+\alpha}Ax(t) + a_2 D^{1+\alpha}\left(\xi(t) - \hat{\eta}\right) \\ -\left[a_3\sigma_c(x) + a_4\mathrm{sgn}(\sigma_c(x))\right]\end{bmatrix}$$

$$\Rightarrow \dot{V}_2(\sigma_c(x)) = \sigma_c(x)\left\{a_2 D^{1+\alpha}\left(\xi(t) - \hat{\eta}\right) - \left[a_3\sigma_c(x) + a_4\mathrm{sgn}(\sigma_c(x))\right]\right\} \quad (37)$$

Box I.

Solving Eqs. (33) and (36), we get, Eq. (37) given in Box I. Defining, $e_d(t) = \left(\xi(t) - \hat{\eta}\right)$, Eq. (37) can be simplified as

$$\begin{cases}\dot{V}_2(\sigma_c(x)) = \sigma_c(x)\left[-a_3\sigma_c(x) - a_4\mathrm{sgn}(\sigma_c(x)) + a_2 D^{1+\alpha}e_d(t)\right] \\ \Rightarrow \dot{V}_2(\sigma_c(x)) \le -a_3\sigma_c^2(x) - \left[a_4 - a_2 D^{1+\alpha}e_d(t)\right]|\sigma_c(x)|\end{cases} \quad (38)$$

Since $\sigma_c(x) > 0$, $\dot{V}_2(\sigma_c(x)) \le 0\ \forall \sigma_c(x) \ne 0$. Thus, invoking Theorem 1, it may be concluded that the chosen sliding surface of FOSMC is asymptotically stable, which implies fast convergence of state trajectories to equilibrium point in finite time.

4. Results and comparative study

In this section, the dynamic performance of hy-WD-PS (test system-1) has been closely inspected employing the proposed adaptive FO-SM-DOB aided FOSMC. The developed resilient fractional-order nonlinear controller regulates the blade pitch angle of the WTs rotor, and subsequently, controls the frequency output of hy-WD-PS. Moreover, to quantify the mastery of the designed controller, the performances of a highly nonlinear open-loop unstable magnetic levitation (MagLev) have been studied. A tracking control problem has been framed to assess the superiority of the designed controller over other prevalent controllers of state-of-art. Further, the effectiveness of the proposed control strategy has been validated on an IEEE 39-bus New England large dimensional power system. The models of test systems are developed on a SIMULINK platform (MATLAB R2013a). Extensive simulation studies have been performed and discussed in the subsequent sections to measure the supremacy of the proposed controller in terms of speed of responses, weaker chattering, disturbance rejection ability, and tracking characteristics.

Table 1
Optimized gains of PID/FOPID controller and minimum fitness function value employing CCSA.

Controllers	k_p	k_i	k_d	N	λ	J
PID	0.0286	0.1150	−1.1222	112.9256	–	0.0784
FOPID	0.3457	0.5226	−1.3175	173.2289	0.4161	0.0719

λ: Fractional-power of integrator of FOPID controller.

4.1. Dynamic performance assessment of hy-WD-PS (test system-1)

4.1.1. Performance study under constant perturbations

Initially, a constant wind power perturbation and load variation of 0.01 puMW each are applied to investigate the dynamic performance of hy-WD-PS. To measure the effectiveness of the proposed control algorithm, system performances have also been studied with integer/FO PID controller, integer/FO SMC (without DOB), full-order state observer-based SMC (SOB-SMC), and second-order SMC (SOSMC). The design of SOB-SMC and SOSMC following the stability analysis using the Lyapunov argument is presented in Appendices C and D, respectively.

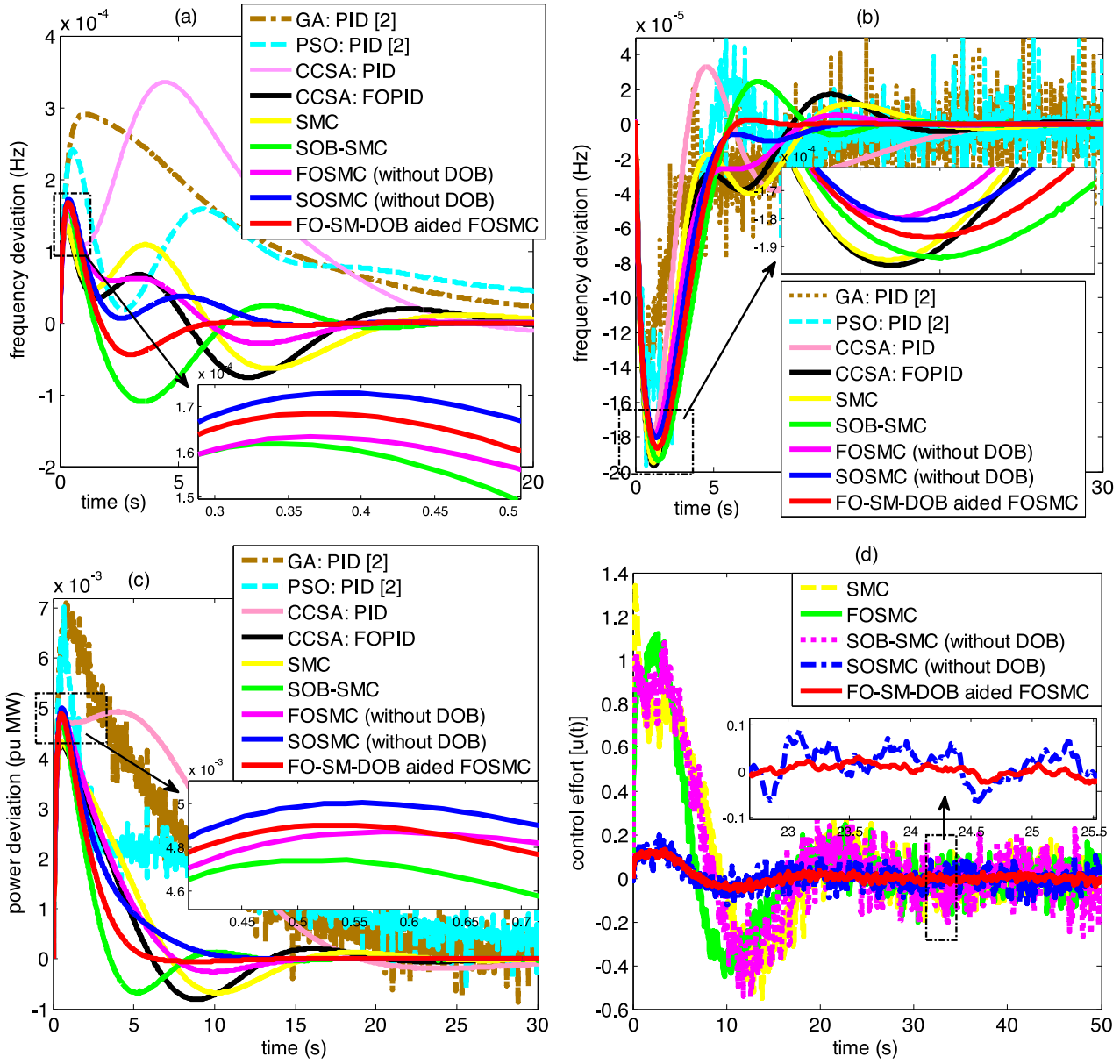

Fig. 4. Dynamic performance of hy-WD-PS subjected to constant perturbations (a) frequency deviation of wind power generator, (b) frequency deviation of DEG, (c) power deviation (ΔP_{WDG}), (d) control effort.

Table 2
Qualitative analysis of hy-WD-PS output following constant perturbations.

Controllers	$\Delta\omega_1$			$\Delta\omega_2$			ΔP_{WDG}		
	OS ($\times 10^{-4}$)	US ($\times 10^{-5}$)	ST	OS ($\times 10^{-6}$)	US ($\times 10^{-4}$)	ST	OS	US ($\times 10^{-4}$)	ST
GA:PID [2]	2.92	**0**	30	72.4	**1.503**	–	0.0071	12	–
PSO:PID [2]	2.42	0.0304	51.9	64.8	1.97	–	0.0070	10	–
CCSA:PID	3.36	1.2667	28.506	33.19	1.81	21.20	0.0049	1.89	30.05
CCSA:FOPID	**1.37**	7.56	24.49	17.17	1.97	20.504	**0.0043**	8.07	19.05
SMC	**1.37**	6.32	21.263	11.73	1.95	17.56	**0.0043**	6.751	20.89
SOB-SMC	1.618	10.97	12.186	24.66	1.94	40.09	0.0047	6.819	11.71
FOSMC (without DOB)	1.63	2.85	12.53	5.18	1.79	14.64	0.0049	0.254	13.16
SOSMC (without DOB)	1.73	0.268	8.53	**0**	1.805	11.3	0.0050	**0**	9.71
FO-SM-DOB aided FOSMC	1.68	4.38	**5.88**	2.71	1.87	**6.06**	0.0049	0.497	**5.47**

[FOPID: Fractional-order PID; FOSMC: Fractional-order SMC; SOB-SMC: State observer-based SMC; GA: Genetic algorithm; PSO: Particle swarm optimization].
The entry "–" implies not settled to final value.

Furthermore, the outputs of the system obtained with the proposed controller are also compared with GA/PSO-tuned PID controllers [2], considering the identical test system. Chaotic crow search algorithm (CCSA) has been considered to explore the near-optimum gains of integer/FO PID controllers, exercising integral time absolute error (ITAE)-type fitness function defined

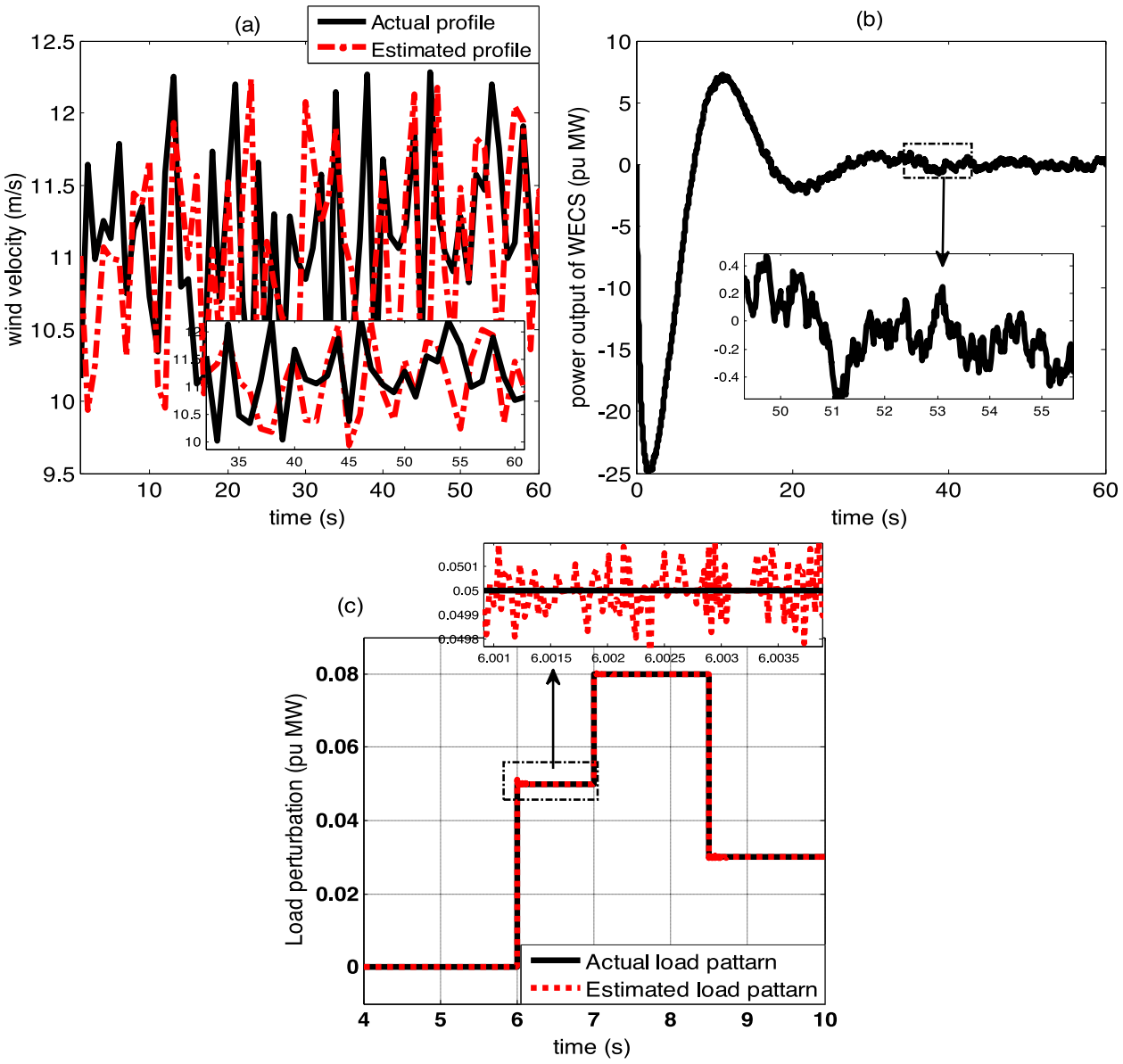

Fig. 5. Plant disturbances (a) wind velocity, (b) output power (electrical) of WECS, (c) multi-step load profile.

in Eq. (39).

$$J = \int_{t=0}^{T_{sim}} (|\Delta\omega_1| + |\Delta\omega_2| + |\Delta P_{WDG}|) \times t \times dt \tag{39}$$

where T_{sim} is the simulation time which is considered as 100 for parameters optimization. For the algorithmic steps of CCSA, readers can refer to [14]. The near-optimum gains of integer/FO PID controller [within the search boundary (−2,+2)] and the minimum value of the fitness function are presented in Table 1.

Fig. 4 shows the system outputs, *i.e.*, frequency deviation of WPG ($\Delta\omega_1$), frequency deviation of DEG ($\Delta\omega_2$), power deviation (ΔP_{WDG}), and control effort ($u(t)$). It is evident from Fig. 4 that all the applied controllers can retain the nominal performance of the system following system disturbances. The qualitative assessment of $\Delta\omega_1$, $\Delta\omega_2$, and ΔP_{WDG} in terms of peak overshoot (OS), undershoots (US) and settling time (ST) is provided in Table 2.

Conventional SMC and SOB-SMC fail to quickly drive the output states to the desired equilibrium point. However, the peaks of the frequency responses are small compared with the proposed control approach. It is obtainable from Table 2 and Fig. 4 that the proposed controller significantly improves the speed of the responses and drives the output to speedily attain the steady-state value compared to other control methodologies shown in Fig. 4. It is seen from Fig. 4(d) that all the studied SMC variants have resultant chattering at the control law due to the switching gain of the discontinuous control law. However, the chattering at the controller output is significantly suppressed with SOSMC compared with SMC, FOSMC, and SOB-SMC. The presented comparison shows that with the developed adaptive FO-SM-DOB aided FOSMC, chattering at the SMC's output further reduces without sacrificing the degree of robustness. Both SOSMC and proposed adaptive FO-SM-DOB aided FOSMC satisfactorily compensate the disturbance effects; however, the proposed control approach exhibits faster state convergence to steady-state value than SOSMC.

4.1.2. Performance study against uncertain wind power and constant load perturbations

In this phase, the effectiveness of the proposed resilient fractional-order nonlinear controller is assessed by applying uncertain wind power perturbation (WPP) and constant load

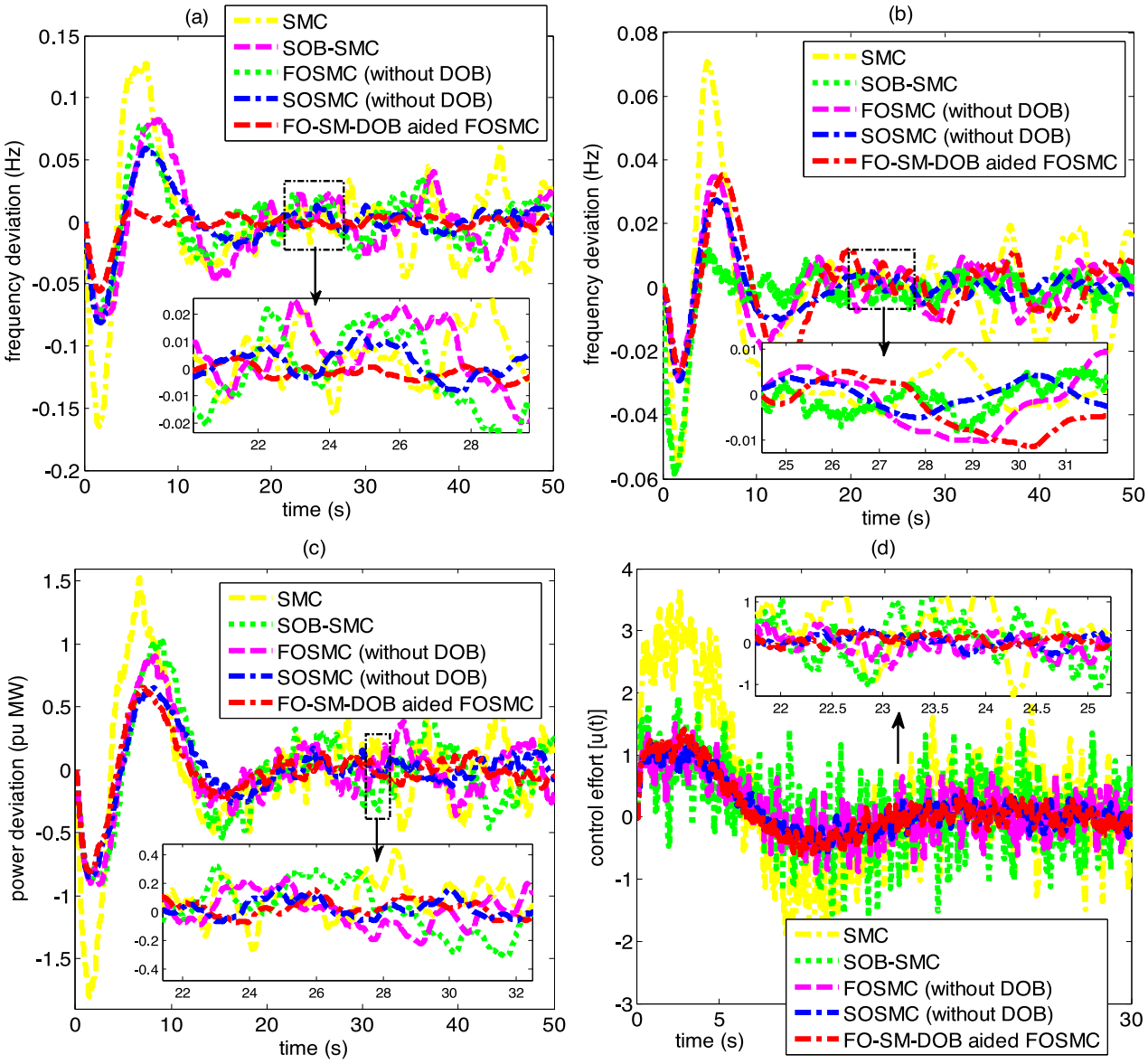

Fig. 6. Dynamic performance of hy-WD-PS subjected to constant load and uncertain WPP (a) frequency deviation of wind power generator, (b) frequency deviation of DEG, (c) power deviation, (d) control effort.

variation (0.01 puMW). An unsteady but bounded wind velocity varying from 9.8 m/s to 12.3 m/s, as shown in Fig. 5(a), is considered as input to WECS. The developed adaptive FO-SM-DOB is employed to estimate the fast variation of wind speed, and the estimated output is plotted in Fig. 5(a). The observer gain of FO-SM-DOB is obtained using the pole placement approach. It is apparent from Fig. 5(a) that the designed adaptive FO-SM-DOB smoothly estimates fast variation of wind velocity in finite time, which affirms the effectiveness of the developed disturbance observer. The output power deviation of WECS subjected to Fig. 5(a) is shown in Fig. 5(b).

To measure the performance of the designed adaptive FO-SM-DOB aided FOSMC, the system outputs are compared with results obtained utilizing SMC, SOB-SMC, FOSMC (without any DOB), and SOSMC, considering constant load and uncertain wind power perturbations. The system outputs, *i.e.*, $\Delta\omega_1$, $\Delta\omega_2$, and ΔP_{WDG}, are depicted in Fig. 6(a)–(c). It is noteworthy that despite highly uncertain wind power perturbation, all the applied controllers ensure stable operation of hy-WD-PS. Due to the uncertain behaviour of wind power perturbation, system frequency exhibits bounded oscillations at the steady-state level. It is evident from Fig. 6(a)–(c), SMC offers system output with a high peak (OS/US) and deteriorates the nominal dynamic performance of the system. With the designed SOSMC, significant improvement in power–frequency oscillations has been recorded for the undertaken hy-WD-PS compared to SMC, FOSMC, and SOB-SMC. On the other hand, the proposed adaptive FO-SM-DOB aided FOSMC offers fast frequency convergence with minimum peak OS/US to desired equilibrium point than SOSMC. The superiority of SOSMC in chattering elimination over other SMC variants is seen in Fig. 6(d). It is apparent from Fig. 6(d) that the developed FOSMC involving disturbance estimation utilizing adaptive FO-SM-DOB further suppresses chattering in control effort. Hence, from the presented observation, the superiority of the proposed adaptive FO-SM-DOB aided FOSMC has been confirmed against unknown/uncertain system disturbances.

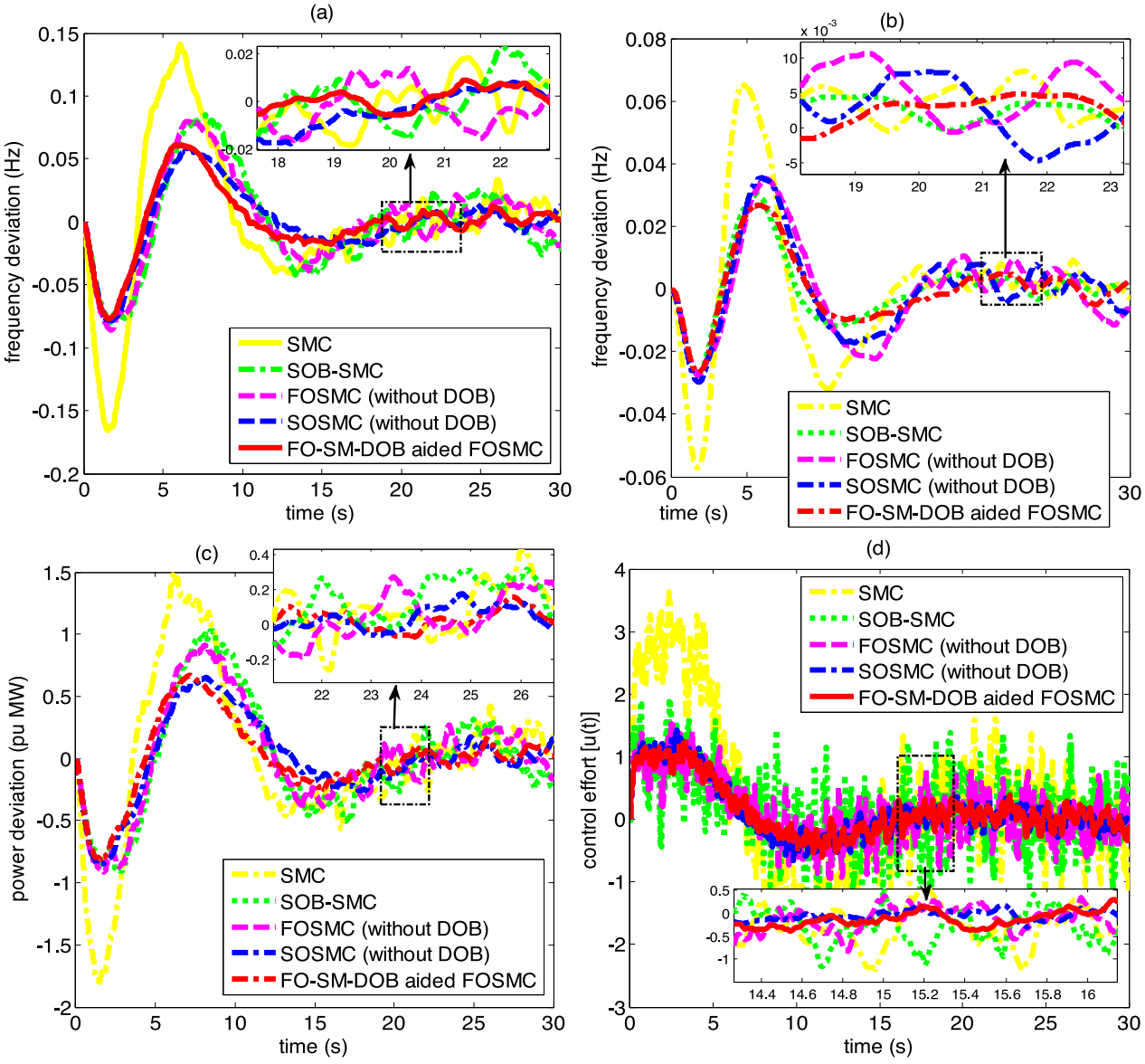

Fig. 7. Dynamic performance of hy-WD-PS subjected to MSLV and uncertain WPP (a) frequency deviation of wind power generator, (b) frequency deviation of DEG, (c) power deviation, (d) control effort.

4.1.3. Performance study against uncertain wind power perturbation and multi-step load variation

A practical power system experiences abrupt load variation. This section examines the disturbance rejection ability of hy-WD-PS under the adaptive FO-SM-DOB aided FOSMC considering uncertain wind power perturbation (WPP) and multi-step load variation (MSLV). Fig. 5(c) depicts the profile of applied MSLV. To measure the competence of the developed adaptive FO-SM-DOB in estimating unknown/uncertain load variation, the estimated output is also plotted in Fig. 5(c). Fig. 5(c) shows that the developed adaptive FO-SM-DOB smoothly tracks the fast-changing load pattern and yields finite time estimation of unknown bounded disturbance. The oscillations at the estimated output are bounded and persist about the vicinity of desired equilibrium level. However, undue oscillations can be minimized by further tuning the adaption gain of adaptive FO-SM-DOB.

Fig. 7 shows the frequency deviation, power deviation and control input to the system following MSLV and uncertain WPP. To quantify the supremacy of the proposed control approach, the system performance has also been studied by applying SMC, SOB-SMC, FOSMC (without DOB), and SOSMC. The comparative results are shown in Fig. 7. It is noticed that frequency/power oscillations increase with the adverse effects of the system disturbance. It is seen from Fig. 7 that all the applied robust controllers effectively handle the impact of the unknown/uncertain disturbances and ameliorate the dynamic performance of hy-WD-PS. SOB-SMC and FOSMC (without DOB) yield nearly matched outputs, while SMC offers high peaks of OS/US in frequency/power deviations. The proposed adaptive FO-SM-DOB aided FOSMC and SOSMC provide better results than SMC, FOSMC and SOB-SMC, with nearly the same peak US and OS. However, the proposed control approach has faster state convergence to desired equilibrium point than SOSMC. Moreover, chattering in control effort is satisfactorily suppressed with the suggested adaptive FO-SM-DOB aided FOSMC without sacrificing the nominal performance of the power system. In summary, the applied resilient fractional-order nonlinear control approach provides a simple and effective way of compensating the unknown plant disturbances and yields a high degree of robustness to the overall closed-loop control system.

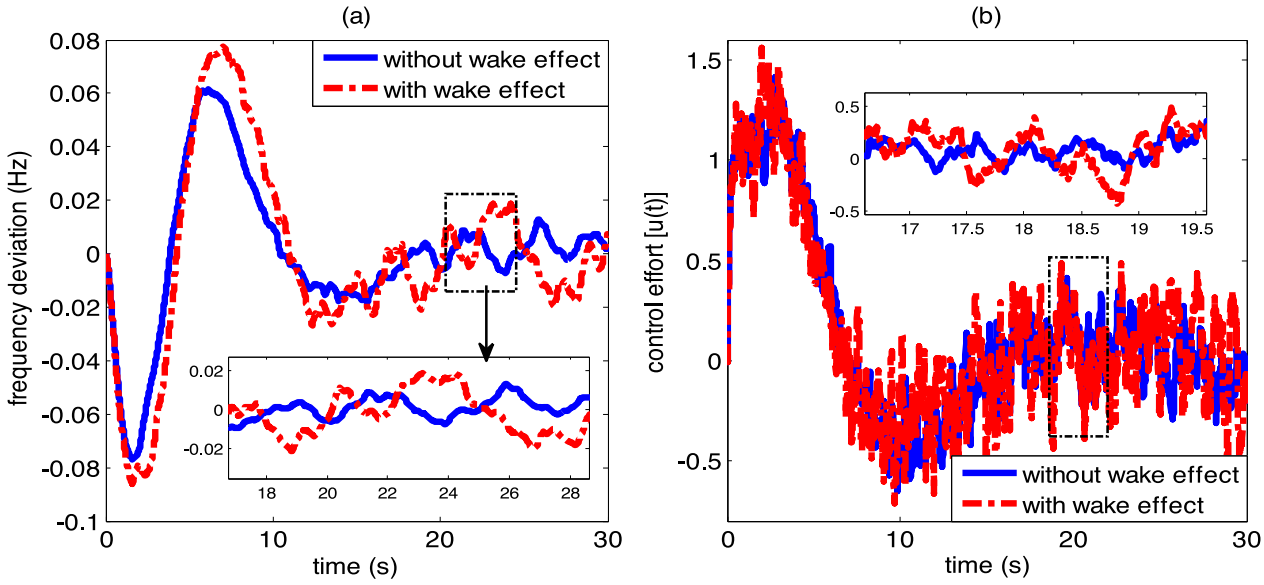

Fig. 8. Dynamic performance of hy-WD-PS considering wake effect in WTs (a) frequency deviation of wind power generator, (b) control effort.

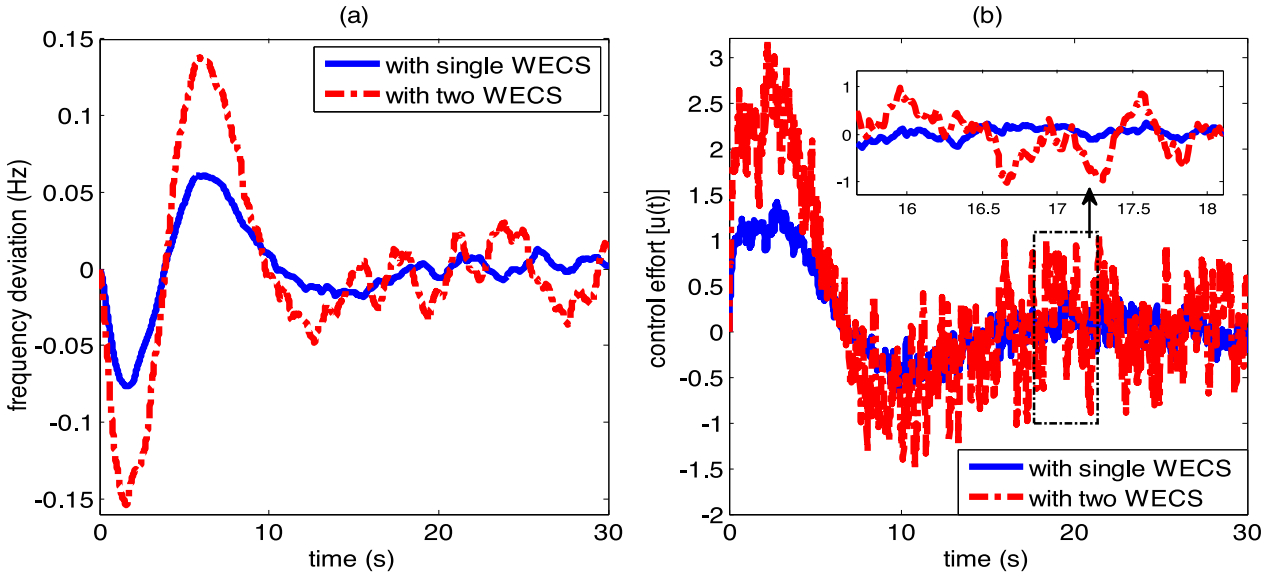

Fig. 9. Dynamic performance of hy-WD-PS with extra WECS penetrated (a) frequency deviation of wind power generator, (b) control effort.

4.1.4. Performance study considering wake effects in WTs

To demonstrate the mastery of the applied control algorithm, the performance of hy-WD-PS has been investigated, considering wake effects in WTs of WECS. The frequency deviation of wind power systems with and without wake effect in WTs is shown in Fig. 8(a). Fig. 8(b) depicts the control effort of the proposed resilient fractional-order nonlinear controller under this operating scenario. It is elicited from Fig. 8(a) that frequency output has deteriorated with high peak OS/US in the presence of wake effects in WTs. As the power generation of WPP decreases with the wake effect in WTs, further droop in frequency has been seen in Fig. 8(a). However, the higher degree of robustness of the overall control system is affirmed with the developed adaptive FO-SM-DOB aided FOSMC. Fig. 8(b) shows that chattering at the controller output is within the permissible bound, which demonstrates the feasibility and efficacy of the applied control approach.

4.1.5. Performance study under excessive penetration of wind power system

This section investigates the superiority of the applied resilient fractional-order nonlinear controller, considering the double penetration of WECS into the studied hy-WD-PS. Fig. 9 illustrates frequency output and control input to the plant under the adaptive FO-SM-DOB aided FOSMC. Due to the low inertia and intermittent nature of the output power of WPG, the frequency output is suffered from undue oscillations with high peak OS/US. With the double penetration of WECS, the frequency response speed is increased, as indicated in Fig. 9(a). Since only a single controller has been applied to handle the adverse effects of high system disturbances, the control effort is significantly increased, as evident from Fig. 9(b). However, the chattering at the controller output is bounded within permissible limits and efficiently countermeasures the system disturbances.

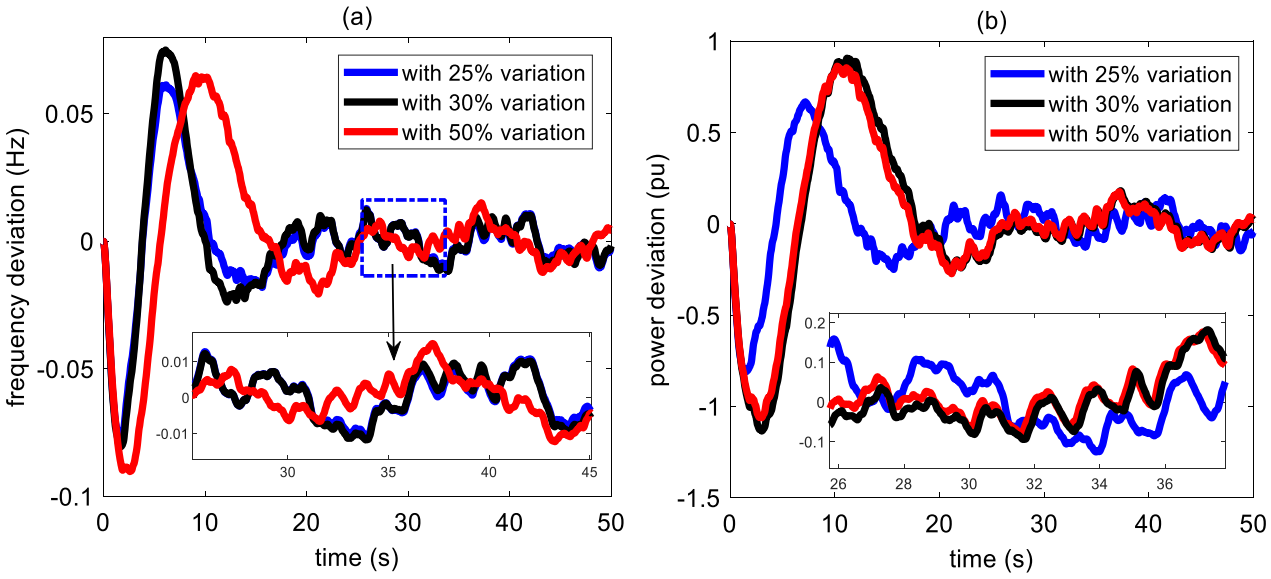

Fig. 10. System dynamics with parameters variation (a) frequency response, (b) power deviation.

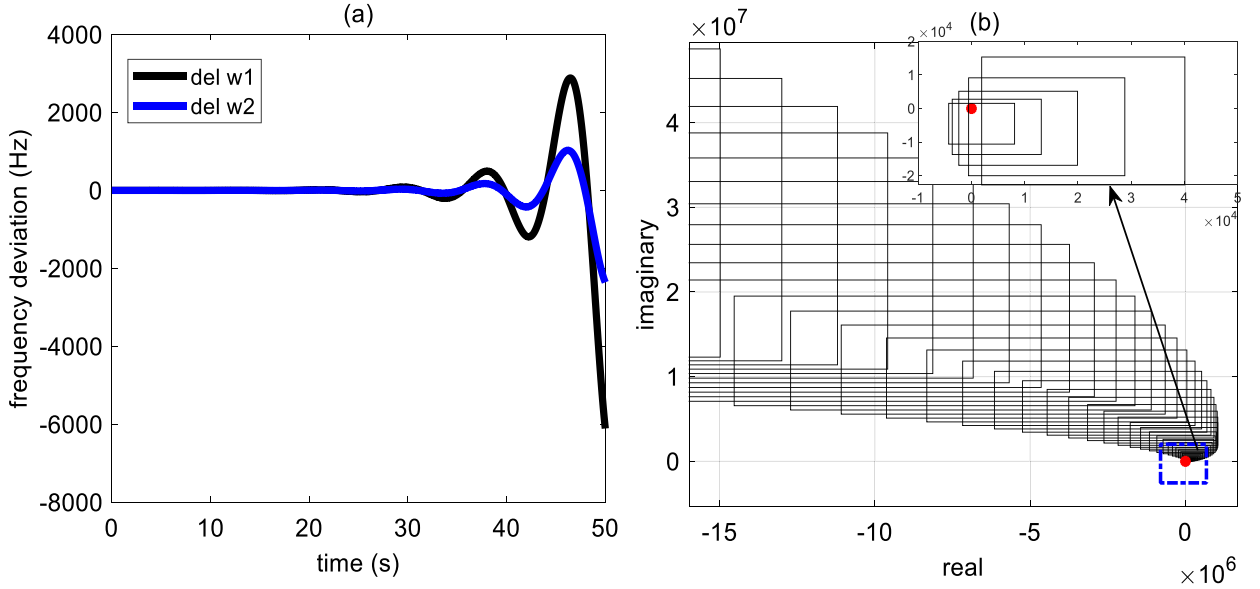

Fig. 11. System dynamics with ±75% variation in system parameters (a) frequency response, (b) Kharitonov's rectangles.

4.1.6. Sensitivity analysis

As discussed in Section 2, ±25% variation in system parameters has been considered to design the proposed resilient fractional-order nonlinear controller for test system-1. In this section, an extensive simulation study has been performed to quantify the sensitiveness of the proposed control methodology to system parameters variation. To perform this analysis, ±30% and ±50% variation in parameters are individually considered, and system performances are obtained under the controller designed in Section 3 [Eq. (33)]. The frequency and power variations for the above-mentioned parametric uncertainty levels are shown and compared in Fig. 10. It is elicited from the presented results that the designed controller works robustly without much worsening the speed and shaping of dynamic responses. Fig. 10 clearly shows that the controller designed with ±25% variation in system parameters is competitively superior, robust, and stable against ±30% and ±50% changes in system parameters. Thus, the resiliency of the developed closed-loop control system is affirmed against wide parameter changes.

Further, to check the stability margin of the closed-loop system against parametric uncertainty, an empirical study is also carried out by changing the variation level (±5% in step). Analysis reveals that the system loses stability if parameters vary between ±75% from nominal settings. The frequency deviation of test system-1 with ±75% parameters variation is plotted in Fig. 11(a), which shows that responses become unbounded. Moreover, Kharitonov's stability test is also performed to check the closed-loop stability with ±75% parameters variation, and the result is shown in Fig. 11(b). It is noteworthy from Fig. 11(b) that Kharitonov's rectangles included the origin, demonstrating the instability of the closed-loop system [48]. Hence, it may be concluded that the system is robustly unstable if parameters vary between ±75% from nominal settings. However, in small-signal stability analysis of power systems, this type of wider variation

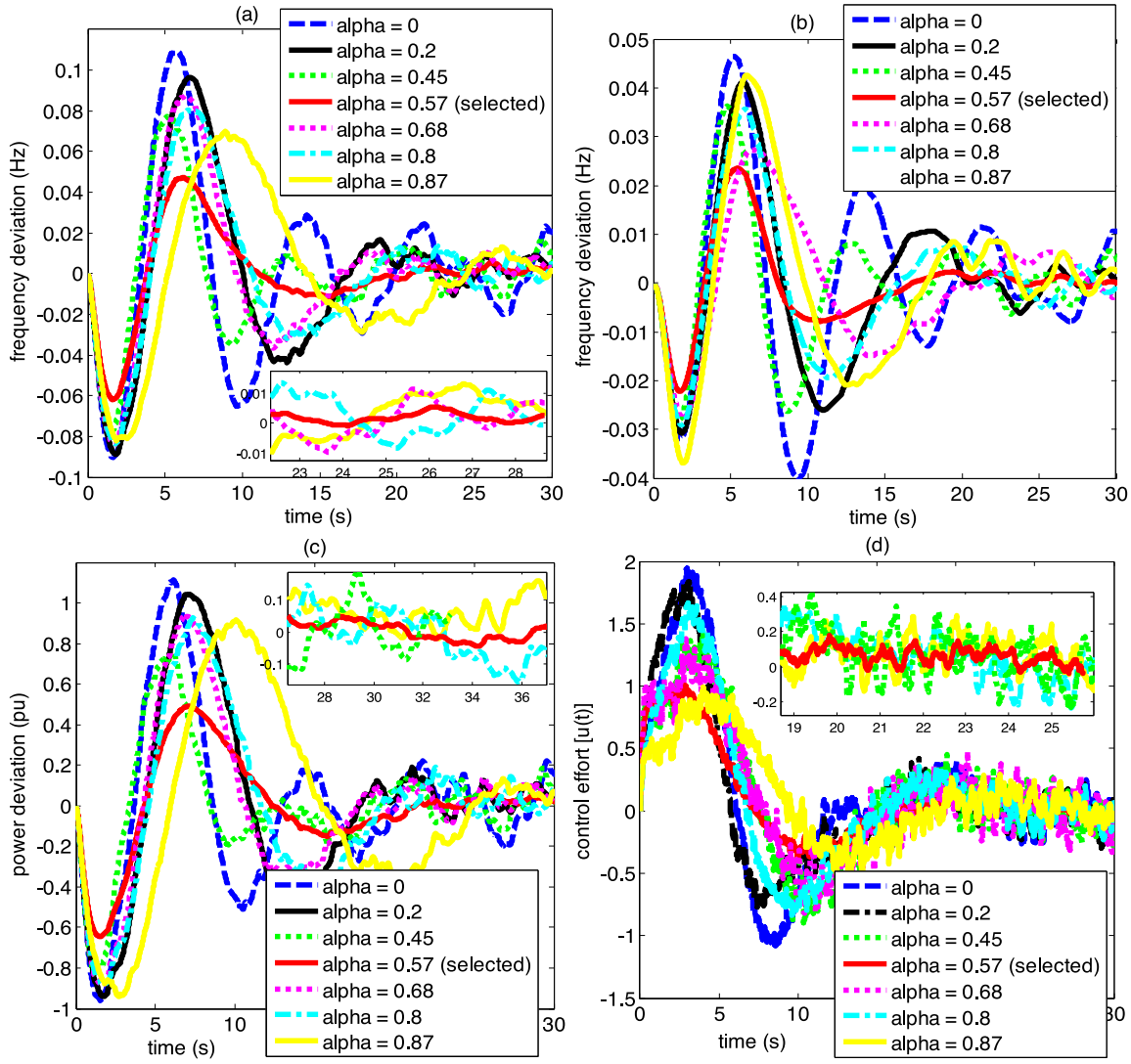

Fig. 12. Effect of fractional power value (α) on the system outputs (a) frequency deviation of WPG, (b) frequency deviation of DEG, (c) power deviation, (d) control effort.

in system parameters is minimal. Due to page limitations, the results of the empirical study are not shown.

4.1.7. Effect of fractional power value (α) on the system performance

Furthermore, to demonstrate the effect of fractional power value (α) of FOSMC, the dynamic stability of test system-1 following uncertain wind power perturbation and multi-step load variation is investigated. The system performance has been measured for different values of α and illustrated in Fig. 12. Fig. 12 shows the frequency deviation of WPG and DEG, power deviation and control effort. As seen in Fig. 12, if $\alpha = 0$, the controller works under proportional logic, and system outputs suffer from high peaks and poor damping in power–frequency oscillations. Controller output also suffers from high chattering. With increasing α, the disturbance rejection ability of the controller increases and shaping of responses improves adequately, *i.e.*, responses become faster with less frequency nadir. Moreover, chattering in control effort is also reduced. It is also seen from the figure that with increasing α (close to unity), the designed controller works under proportional–derivative logic. As a result, the damping in the system output improves but suffers from sluggishness. Based on the presented empirical results (Fig. 12), $\alpha = 0.57$ is selected as the fractional power value of FOSMC to assess system dynamics.

4.2. Performance assessment of magnetic levitation (MagLev) system (test system-2)

This section focuses on assessing the performance of the proposed resilient fractional-order nonlinear controller applied to a highly nonlinear open-loop unstable MagLev system. MagLev system, used for frictionless motion of an object, comprises electromechanical and electrical subsystems. It generates an eddy-current effect by metal objects under the action of high-frequency electromagnetic fields to suspend an object stably in the air [50–52]. The dynamical model of the MagLev system considered for the study in state–space form can be expressed as [51,52]

$$\begin{cases} \dot{x}_1 = x_2 \\ \dot{x}_2 = -\dfrac{K_m x_3^2}{2M_b x_1^2} + g \\ \dot{x}_3 = -\dfrac{(R_c + R_s)}{L_c} x_3 + \dfrac{1}{L_c} u \end{cases} \tag{40}$$

where $x \in \mathbb{R}^{3\times 1}\left(= \begin{bmatrix} x_b & \dot{x}_b & I_c \end{bmatrix}^T\right)$ is the state variable; $u\,(= V_c)$ represents the control input; x_b represents the air-gap between the ball and the electromagnetic force; K_m is electromagnetic

force constant; g is gravitational acceleration; M_b defines the mass of the ball; L_c is the inductance of the coil; R_c, R_s are the coil resistance and current sense resistance, respectively. For more details on the mathematical description of MagLev system, readers can refer to [51,52]. In [50], the performance of FOSMC has been assessed for MagLev system and compares the results with SMC. However, this work assumes that gradients of disturbance are available, which is difficult to compute in practice.

In this section, the controller performance has been measured by formulating a tracking control problem considering endogenous and exogenous system disturbances. The error dynamics of the system defined in Eq. (40) can be formulated as [51,52]

$$\begin{cases} \dot{\varepsilon}_1 = \varepsilon_2 \\ \dot{\varepsilon}_2 = -a_1\varepsilon_1 - a_2\varepsilon_2 + x_3^d + d_1 \qquad [a_1 > 0, a_2 > 0] \\ \dot{\varepsilon}_3 = -a_0 x_3 + b_0 u + d_2 \end{cases} \tag{41}$$

where

$$\begin{cases} a_0 = \left(R_{c,\text{nominal}} + R_{s,\text{nominal}}\right)/L_{c,\text{nominal}};\ \ b_0 = 1/L_{c,\text{nominal}} \\ a = \left(R_c + R_s\right)/L_c;\ \ b = 1/L_c; \\ d_1 = a_1\varepsilon_1 + a_2\varepsilon_2 - \dfrac{K_m x_3^2}{2M_b x_1^2} + g - x_3^d - \ddot{\bar{r}} \\ d_2 = -\left(a - a_0\right)x_3 + \left(b - b_0\right)u - \left(\dot{x}_3^d\right) \end{cases} \tag{42}$$

In Eq. (42), d_1, d_2 are the exogenous disturbances; $R_{c,\text{nominal}}$, $R_{s,\text{nominal}}$, and $L_{c,\text{nominal}}$ show the nominal values of R_c, R_s, and L_c. The respective tracking errors (time-varying) shown in Eq. (41) are computed as

$$\begin{cases} \varepsilon_1(t) = \left\{x_1(t) - x_1^d(t)\right\} \\ \varepsilon_2(t) = \left\{x_2(t) - x_2^d(t)\right\} \\ \varepsilon_3(t) = \left\{x_3(t) - x_3^d(t)\right\} \end{cases} \tag{43}$$

where $x_1^d(t)$ is the desired ball position; $x_2^d = \dot{x}_1^d$; x_3^d represents the desired current through the coil.

Control objective: Design a control law $u(t)$ such that ball position (x_b) in the air follows a reference trajectory $x_1^d(t)$ and the current through the magnetic coil ($x_3(t)$) can be limited within the permissible limit $\left(i.e.,\ x_3^d(t)\right)$ subjected to system uncertainties. In other words, the controller design is to emphasize $\varepsilon_1 \to 0, \varepsilon_2 \to 0,$ and $\varepsilon_3 \to 0$, as $t \to \infty$.

The developed adaptive SM-FO-DO is utilized to estimate the lumped plant uncertainty (unknown boundary value $\hat{\eta}$), including parameters variation and exogenous disturbances. For studying the controller performance, ±2% variation in system parameters from nominal value (provided in Appendix A), *i.e.*, K_m, M_b, R_c, R_s, L_c, is considered [51]. The chosen fractional-type sliding manifold ($\sigma(t)$) and computed control law for the MagLev system [Eq. (40)] to maintain the desired electromagnetic field, *i.e.*, for regulating the coil current, are given in Eqs. (44)–(45), respectively. The controller is designed under the assumption that all the state variables are available for measurement.

$$\sigma(t) = \kappa_1\varepsilon_3(t) + \kappa_2 D^{\alpha-1}\varepsilon_3(t) \qquad \kappa_1 > 0, \kappa_2 > 0 \tag{44}$$

$$u(t) = -\left(\kappa_1 b_0\right)^{-1}\left[-\kappa_1 a_0 x_3 + \hat{\eta} + \kappa_2 D^{\alpha}\varepsilon_3 + \kappa_3\sigma(t) + \kappa_4 \text{sgn}\left(\sigma(t)\right)\right] \tag{45}$$

where $\kappa_1, \kappa_2, \kappa_3, \kappa_4$ are the design parameters of FOSMC. The closed-loop stability utilizing the Lyapunov argument is validated and presented in Appendix E. The design parameters of FOSMC by trial-and-error are computed as

$$\begin{cases} \kappa_1 = \begin{bmatrix} -99.5124 & -0.8901 & 1 \end{bmatrix} \\ \kappa_2 = \begin{bmatrix} 0.324 & 0.0518 & 0.4235 \end{bmatrix} \\ \kappa_3 = 0.202 \\ \kappa_4 = 0.3907 \\ \alpha = 0.71 \end{cases} \tag{46}$$

4.2.1. Performance analysis of the controller

The mathematical model of MagLev system [Eq. (40)] is developed on MATLAB environment to carry out the analysis. The initial conditions of the states are assumed as $x(0) = \begin{bmatrix} 0.013 & 0 & 1.115 \end{bmatrix}^T$. The reference trajectory, *i.e.*, desired ball position, is considered as $x_1^d = 8$ mm, and the current through the magnetic coil is limited to $x_3^d = 0.75$ A.

The system outputs with the developed adaptive SM-FO-DOB-aided FOSMC are shown in Fig. 13. The results obtained with the proposed controller are compared with SMC and FOSMC [50]. Fig. 13(a) shows the position of the ferromagnetic ball suspended freely and stably in the air with SMC [50], FOSMC [50], and the proposed controller. It is seen from the figure that all the designed controllers can retain stability following system disturbances and ensures good tracking of reference input. It is worthy to note that the proposed adaptive SM-FO-DOB-aided FOSMC gives good tracking with fast convergence and the least steady-state error compared to FOSMC (without DOB). The same conclusion may be drawn from Fig. 13(b). Fig. 13(c) shows that the current required to achieve the desired tracking characteristic is within the maximum permissible limit under the designed control action. It is worthy to note that the coil current speedily converges to the final value (0.75 A) under the proposed adaptive FO-SM-DOB aided FOSMC compared to SMC [50] and FOSMC (without DOB) [50]. It also offers minimum steady-state error as compared with FOSMC. Hence, from the presented results, it may be concluded that the developed resilient fractional-order nonlinear controller is competent to levitate the magnetic ball at the desired position in the air freely and stably against unknown/uncertain system uncertainties.

The control effort (voltage control law) is plotted and compared in Fig. 13(d). It is revealed from Fig. 13(d) that SMC yields a high transient peak with chattering. With the integration of FO calculus, chattering at SMC output is satisfactorily attenuated. Moreover, the proposed resilient fractional-order nonlinear controller offers less control effort to speedily converge system states to the steady-state than FOSMC (without DOB). Hence, it may be concluded that with the augmentation of designed adaptive FO-SM-DOB into FOSMC, state convergence has been significantly increased, and chattering is also effectively attenuated.

4.2.2. Effect of fractional power value (α) on the system performance

In this section, an empirical study has been conducted to assess the effect of fractional power value (α) on the MagLev system outputs. For different values of α, MagLev outputs, *i.e.*, ball position and current through the coil, are plotted and compared in Fig. 14(a) and (b), respectively. It is seen from the presented results that with increasing α, the peak of the responses is increased, and states slowly converge to steady-state levels. From the voltage control law plotted in Fig. 14(c), it is elicited that chattering increases with increasing α. The undertaken MagLev system [Eq. (40)] becomes unstable for $\alpha < 0.67$. Hence, from the presented results, it may be concluded that MagLev system output is susceptible to the fractional power value α of FOSMC. For the present study, the best value of α is set at 0.71, as it yields optimum results.

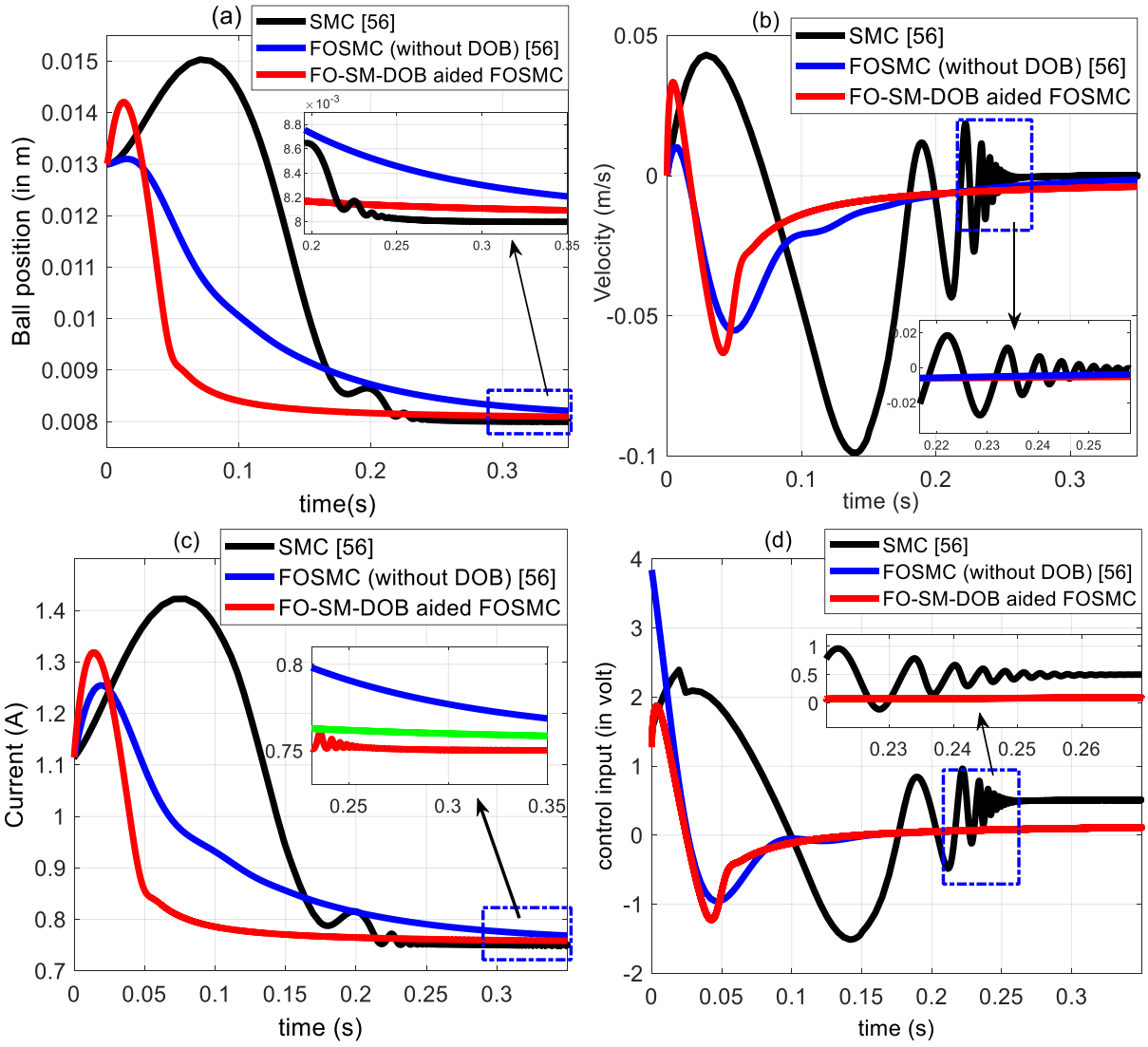

Fig. 13. Outputs of MagLev system (a) ball position (x_1), (b) velocity of ball (x_2), (c) current through the coil (x_3), (d) voltage control effort (u).

4.3. Controller performance analysis for IEEE 39-bus new England system having WPG integrated (test system-3)

In this section, an IEEE 39-bus New England power system depicted in Fig. 15(a) is considered to further demonstrate the effectiveness of the designed resilient fractional-order nonlinear controller. The studied IEEE 39-bus New England power system comprises 10 generators, 19 loads, 34 transformers, and 12 transmission lines. The 39-bus system is grouped into three areas, as shown in Fig. 15(a). Area-1 includes Gen-1, Gen-2, and Gen-3. Area-2 includes Gen-8, Gen-9, and Gen-10, and Gen-4, Gen-5, Gen-6, and Gen-7 are grouped into area-3 [53,54]. All the generators in the respective area are operated in parallel. The connected loads in area-1, area-2, and area-3 are 265.5 MW, 233 MW, and 125 MW, respectively, and the total power generation is 842 MW [54]. To critically analyse the performance of the proposed controller, the modelled WPG of 3.6 MW is penetrated at bus-31 in area-1 and bus-36 in area-2. For system parameters, readers can refer to [53].

The performance of the proposed adaptive FO-SM-DOB aided FOSMC is reviewed against random step load variation in individual areas. The frequency deviation of area-1 and area-3 are shown in Fig. 15(b) and (c), respectively. Moreover, to confirm the efficacy of the proposed adaptive FO-SM-DOB aided FOSMC, the dynamics of IEEE 39-bus system are also analysed under SOSMC (without DOB) and FOSMC (without DOB), and compared in Fig. 15. It is noted from Fig. 15(b)–(c) that the suggested adaptive FO-SM-DOB aided FOSMC significantly improves transient performance as compared to SOSMC/FOSMC. The results illustrate that with adaptive FO-SM-DOB aided FOSMC, frequency oscillation quickly dies down and perturbed states are asymptotically converged to equilibrium point speedily. The proposed adaptive FO-SM-DOB aided FOSMC effectively countermeasures system uncertainty and disturbances and retains the grid stability.

The designed controller can maintain zero tie-line power deviations between areas, as elicited from Fig. 15(d), with minimum peak overshoot/frequency nadir and better steady-state accuracy. It is also noteworthy from Fig. 15(e) that the chattering in control inputs with adaptive FO-SM-DOB aided FOSMC is least compared to SOSMC/FOSMC, which reduces actuator saturation problem (valves of steam turbines) significantly. Hence, from the presented discussion, the superiority and robustness of adaptive FO-SM-DOB aided FOSMC have been affirmed for a large-dimensional complex power system.

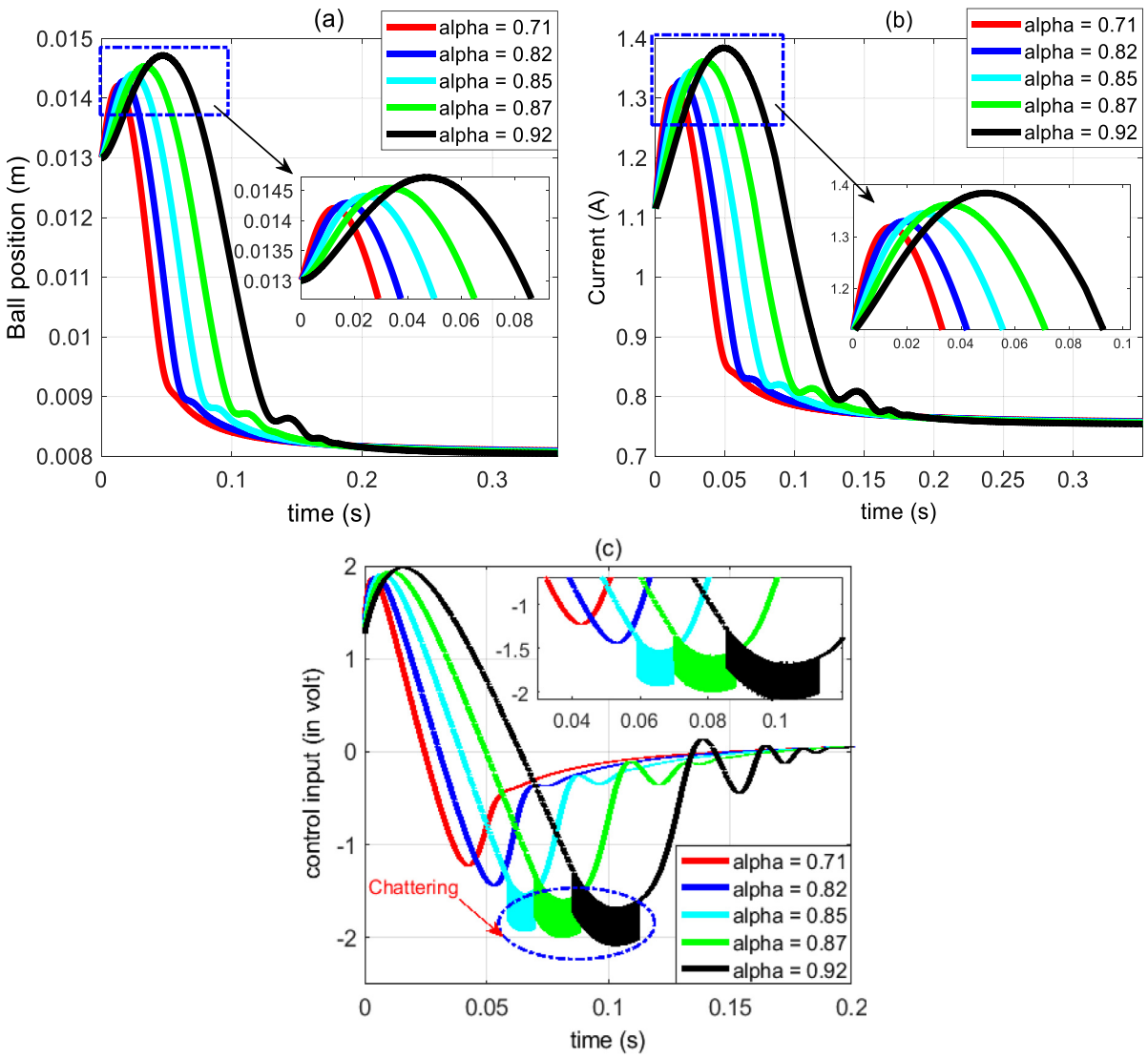

Fig. 14. The effect of fractional power value (α) on the MagLev system outputs (a) ball position (x_1), (b) current through the coil (x_3), (c) voltage control effort (u).

5. Conclusion

This paper has maidenly designed and applied a resilient fractional-order nonlinear controller for theoretical frequency regulation of a hybrid wind–diesel based power system (hy-WD-PS). Initially, an adaptive fractional-order sliding-mode disturbance observer (FO-SM-DOB) is designed to estimate lumped system disturbances, including exogenous disturbances and parameter uncertainty. Subsequently, an improved FOSMC is realized by augmenting this estimation for effectively attenuating chattering in control law and fast compensation of unknown/uncertain system disturbances. The effectiveness of the applied resilient fractional-order nonlinear controller is demonstrated by performing extensive comparative studies under diverse operating scenarios. Presented results show the supremacy of the developed adaptive FO-SM-DOB aided FOSMC over integer/FO PID controller, integer/FO SMC, SOB-SMC, SOSMC (without DOB), and the results reported in the literature in terms of attenuation of chattering in control effort and betterment of nominal performance of hy-WD-PS. The presented results affirm the effectiveness of the proposed resilient fractional-order nonlinear controller in coping with modelling error, parameter uncertainty, and unknown bounded system disturbances. Later, a highly nonlinear open-loop unstable magnetic levitation system is considered to analyse the effectiveness of the designed controller. Results show that the proposed controller is competent to countermeasure unknown/uncertain system disturbances and gives satisfactory tracking performance of the MagLev system. Presented results further establish the efficacy of adaptive FO-SM-DOB in reducing chattering at the controller output. Furthermore, the designed adaptive FO-SM-DOB aided FOSMC is tested on an IEEE 39-bus New England power system, and dynamic stability has been assessed following random load perturbations. The presented results not only showed the resiliency of the designed controller but also can be successfully implemented in a large dimensional power system. However, selecting appropriate gains of design parameters of the proposed controller is computationally intensive and requires deep knowledge. Table 3 presents a brief comparative study between the proposed controller and other prevalent controllers of state-of-art.

5.1. Future scope

In line with the presented control methodology, the following may be considered as a future extension of the work:

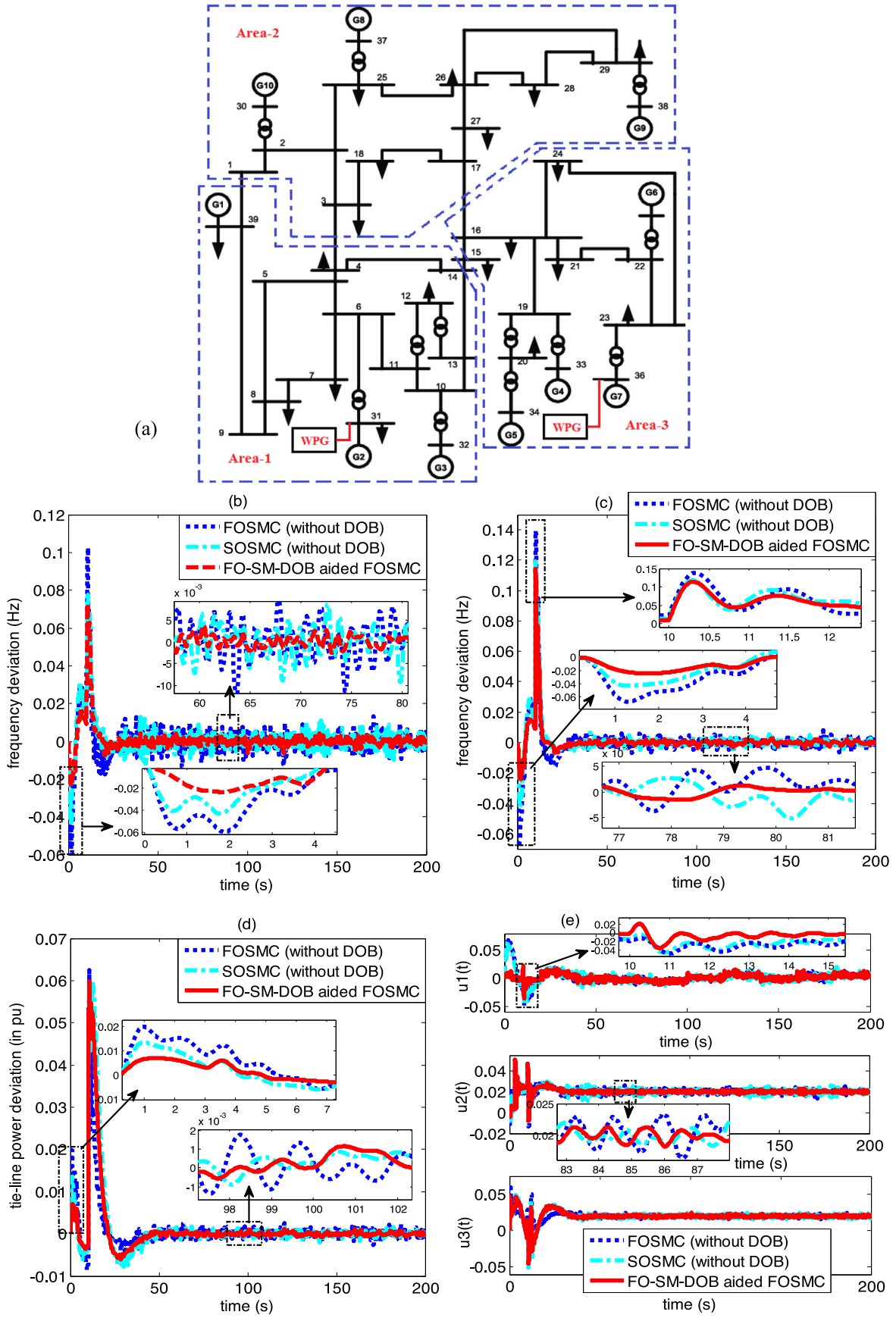

Fig. 15. (a) Single line diagram of IEEE 39-bus New England system, (b) frequency deviation in area-1, (c) frequency deviation in area-3, (d) tie-line power deviation between area-1 and area-3, (d) control inputs.

Table 3
Pros and cons of the developed resilient fractional-order nonlinear controller.

Sl. No.	Control techniques	Tuning parameters	Disturbance rejection ability	Chattering	Robust degree of Stability	Design complexity	Computational complexity
1	PID	Less parameters to be tuned	Poor	Not seen in the control law (linear control action)	Performance deteriorates with system uncertainties (Less robust)	Straightforward design	Simple structure and easy implementation
2	FO-PID	Extra fractional power settings to be tuned	Improved compared to PID because of higher controller degree-of-freedom	Not seen in the control law (linear control action)	Robustness improved with integration of FO-calculus	Complex design	Tuning of additional fractional settings requires more computation time
3	SMC	Less parameters to be tuned (state feedback and switching gains)	High disturbance rejection ability	Suffered from high chattering in the control law.	Robust against system uncertainties	Straightforward design	Computationally simple
4	State observer-based SMC	In addition to Sl. No. (3), observer gain needs to be tuned	High disturbance rejection ability	Suffered from high chattering in the control law.	Robust against system uncertainties	Simple design	Computationally simple
5	DO-SMC	In addition to Sl. No. (3), observer gain needs to be tuned	Disturbance rejection ability is improved by augmenting disturbance estimation	Chattering reduces with augmentation of disturbance estimation.	Robust against system uncertainties	Simple design	Computationally intensive
6	FO-SMC	Extra fractional power settings to be tuned	High disturbance rejection ability because of increasing degree-of-freedom	Damping in system responses improves, but control effort suffers from chattering	Robust against system uncertainties	Complex design	Computationally intensive
7	Proposed resilient fractional-order nonlinear controller	Compared to others, tuning parameters are more	Disturbance rejection ability significantly improved by augmenting disturbance estimation, adaptiveness, and increasing controller's degree-of-freedom	Improves speed of the responses with less oscillation. Chattering in the control effort is also significantly attenuated.	Introduction of disturbance estimation utilizing SM-DOB and FOC makes closed-loop control system robust and ensures fixed-time state convergence.	Complex design	Computationally intensive

(i) The developed FO-SM-DOB cannot yield robust asymptotic convergence of estimation error for time-varying disturbances. Moreover, it cannot completely eliminate the chattering at controller output, as the switching gain of discontinuous control law sets greater than the upper bound of unknown disturbances. Sliding mode (SM)-based DOB may be realized by introducing an internal model principle to ensure (a) small switching gain (weaker chattering) and (b) guaranteed asymptotic convergence of time-varying disturbance estimation error. In SM-based DOB integrated with internal model principle, switching gain of discontinuous control law needs to be set only greater than the bound on the error of difference $\left(\left|d-\hat{d}\right|\right)$, rather than the whole disturbance signal.

(ii) The design and analysis of the backstepping sliding mode controller for the undertaken hy-WD-PS may be a future extension of the present work.

(iii) With the growing interest in network-based control systems, the frequency regulation problem of the hybrid power system may be studied under cybersecurity framework against cyber threats or bad-data injection.

(iv) The pole placement approach has been considered in this article to obtain the design parameters of the proposed resilient fractional-order nonlinear controller. However, meta-heuristic algorithms can be used for fine-tuning of design parameters of the developed controller.

Declaration of competing interest

The authors declare that they have no known competing financial interests or personal relationships that could have appeared to influence the work reported in this paper.

Appendix A

See Tables A.1 and A.2.

Nominal values of test system-1 parameters [1,2,48]

See Table A.1.

Nominal values of test system-2 parameters [51,52]

See Table A.2.

Table A.1

Parameter	Value	Parameter	Value	Parameter	Value	Parameter	Value
Wind aerodynamic							
λ_{opt}	8.68	V_w	16 m/s	A	8495 m^2	ρ	1.296 kg/m^3
D_r	104 m	α_1	0.5176	α_2	116	α_3	0.4
α_4	5	α_5	21	α_6	0.0068	H_w	3.52 s
H_D	8.7 s	K_{pc}	0.08	K_{hp2}	1.25	k_{fc}	16.2 pu kW/Hz
K_{ph3}	1.4	T_{hp1}	0.6 s	T_{hp2}	0.041 s	K_d	16.5 pu kW/Hz
T_1	0.025 s						
Mechanical coupling shaft and generator							
J_r	4.29 s	J_g	0.9 s	B_{sh}	1.5 pu	N_g	20
K_{tg}	296.7 pu	τ_T	0.1 s	T_{gr}	0.6		

Table A.2

Parameter	Value	Parameter	Value	Parameter	Value	Parameter	Value
R_c	10 Ω	L_c	413 mH	T_b	0.014 m	K_m	6.580×10^{-5} Nm^2/A^2
R_s	1 Ω	M_b	0.068 kg	g	9.81 m/s^2		

$$Plant: \begin{cases} \dot{x}(t) = Ax(t) + Bu(t) + \xi(t) \\ y(t) = Cx(t) \end{cases} \tag{B.1}$$

$$A = \begin{bmatrix}
-\frac{1}{T_{hp2}} & 0 & 0 & 0 & 0 & 0 & 0 & 0 & 0 & 0 & 0 \\
\left(K_{hp2} - \frac{K_{hp2}T_{hp1}}{T_{hp2}}\right) & -1 & 0 & 0 & 0 & 0 & 0 & 0 & 0 & 0 & 0 \\
0 & K_{hp3} & -1 & 0 & 0 & 0 & 0 & 0 & 0 & 0 & 0 \\
0 & 0 & \frac{K_{pc}}{2H_w} & -\frac{K_{fc}}{2H_w} & \frac{K_{fc}}{2H_w} & 0 & 0 & 0 & 0 & 0 & 0 \\
0 & 0 & 0 & \frac{K_{fc}}{2H_d} & -\frac{K_{fc}}{2H_d} & -\frac{1}{2H_d} & 0 & 0 & 0 & 0 & 0 \\
0 & 0 & 0 & 0 & K_d & 0 & 0 & 0 & 0 & 0 & 0 \\
0 & 0 & 0 & 0 & \frac{K_d}{T_1} & \frac{1}{T_1} & -\frac{1}{T_1} & 0 & 0 & 0 & 0 \\
0 & 0 & 0 & 0 & 0 & 0 & 0 & -\left(\frac{D_{WT}+D_{shaft}}{J_{WT}}\right) & \left(\frac{D_{shaft}}{J_{WT}}\right) & -\left(\frac{1}{J_{WT}}\right) & 0 \\
0 & 0 & 0 & 0 & 0 & 0 & 0 & \left(\frac{D_{shaft}}{2J_{gen}}\right) & -\left(\frac{D_{gen}+D_{shaft}}{J_{gen}}\right) & \left(\frac{1}{n_{gear}J_{gen}}\right) & -\left(\frac{1}{J_{gen}}\right) \\
0 & 0 & 0 & 0 & 0 & 0 & 0 & K_{shaft} & -\frac{K_{shaft}}{n_{gear}} & 0 & 0 \\
0 & 0 & 0 & 0 & 0 & 0 & 0 & 0 & 0 & 0 & -\frac{1}{\tau_{gen}}
\end{bmatrix}$$

$$B = \begin{bmatrix} \frac{1}{T_{hp2}} & \frac{K_{hp2}T_{hp1}}{T_{hp2}} & 0 & 0 & 0 & 0 & 0 & 0 & 0 & 0 & 0 \\ 0 & 0 & 0 & 0 & 0 & 0 & 0 & 0 & 0 & 0 & \frac{1}{\tau_{gen}} \end{bmatrix}^T ; \quad G = \begin{bmatrix} 0 & 0 & 0 & \frac{1}{2H_w} & 0 & 0 & 0 & 0 & 0 & 0 & 0 \\ 0 & 0 & 0 & 0 & -\frac{1}{2H_d} & 0 & 0 & 0 & 0 & 0 & 0 \\ 0 & 0 & 0 & 0 & 0 & 0 & 0 & \frac{1}{J_{WT}} & 0 & 0 & 0 \end{bmatrix}^T$$

$$C = \begin{bmatrix} 0 & 0 & 0 & 1 & 0 & 0 & 0 & 0 & 0 & 0 & 0 \\ 0 & 0 & 0 & 0 & 1 & 0 & 0 & 0 & 0 & 0 & 0 \end{bmatrix}$$

Box II.

Appendix B. state–space model of hy-WD-PS

See Eq. (B.1) in Box II.

Appendix C. Design of SOB-SMC and stability analysis

This section presents the design of full-order state observer-based SMC (SOB-SMC) following closed-loop stability analysis

using the Lyapunov argument. Let the dynamics of the observer be

$$\begin{cases} \dot{\hat{x}}(t) = A\hat{x}(t) + Bu(t) + \xi(t) + M\left[y(t) - \hat{y}(t)\right] \\ \hat{y}(t) = C\hat{x}(t) \end{cases} \tag{C.1}$$

where $\hat{x}$ is the estimated state and M is observer gain. Choosing the sliding surface as

$$\sigma(x(t)) = K_1\hat{x}(t) - K_1\left[\int_0^t (A - BK_2)\,\hat{x}(\tau)\,d\tau\right] \tag{C.2}$$

where K_1 & K_2 are the design parameters. Considering the reaching law be

$$\begin{cases} \dot{\sigma} = u_{rch}(t) \\ u_{rch}(t) = \begin{cases} -\dfrac{\sigma}{\alpha\|\sigma\|}\beta - \gamma\sigma; & \|\sigma\| \geq \delta \\ -\dfrac{\sigma}{\alpha\delta}\beta - \gamma\sigma; & \|\sigma\| < \delta \end{cases} \end{cases} \tag{C.3}$$

where $\alpha, \beta, \gamma, \delta > 0$; $\|S\| = \sqrt{\sum_{m=1}^{n}\left|S_m^2\right|}$; n defines the system order/states. The control effort of SMC, based on state estimation is computed as

$$u(t) = -K_2\hat{x}(t) - (K_1B)^{-1}\left[-u_{rch}(t) + K_1\left(\eta + M\left(y - \hat{y}\right)\right)\right] \tag{C.4}$$

Stability Proof:

Let the Lyapunov candidate be

$$V_3(\sigma) = \frac{1}{2}\sigma^2 \tag{C.5}$$

Time derivative of Eq. (C.5) gives

$$\dot{V}_3(\sigma) = \sigma\dot{\sigma} \tag{C.6}$$

Solving Eqs. (C.2) and (C.6), we get

$$\dot{V}_3(\sigma) = \sigma\left[K_1\dot{\hat{x}}(t) - K_1\left((A - BK_2)\,\hat{x}(t)\right)\right] \tag{C.7}$$

Again, solving Eqs. (C.1) and (C.7), we get

$$\begin{aligned} \dot{V}_3(\sigma) = \sigma\Big[&K_1A\hat{x}(t) + K_1Bu(t) + K_1M\left[y(t) - \hat{y}(t)\right] \\ &+K_1\xi(t) - K_1A\hat{x}(t) + K_1BK_2\hat{x}(t)\Big] \end{aligned} \tag{C.8}$$

Substituting $u(t)$ from Eq. (C.4) into Eq. (C.8), we get

$$\dot{V}_3(\sigma) = \sigma\left[u_{rch}(t) + K_1(\xi(t) - \eta)\right] \tag{C.9}$$

Since $(\sigma u_{rch}(t)) < 0$ and $\eta > \xi(t)$, therefore, $\dot{V}_3(\sigma) < 0$. Thus, invoking Lyapunov direct method, it may be concluded that the developed SOB-SMC is asymptotically stable at the equilibrium point.

Appendix D. Design of second-order SMC (SOSMC) and stability analysis

For designing the SOSMC, it is assumed that the pair (A, B) is completely controllable and $|B| \neq 0$. Let the sliding surface be

$$\sigma(x) = K_1x(t) - K_1\left[\int_0^t (A - BK_2)\,x(\tau)\,d\tau\right] \tag{D.1}$$

where K_1, K_2 are the design parameters. The value of K_1 must be selected to meet $|K_1B| \neq 0$, and K_2 must be chosen to satisfy that the eigenvalues of $|A - BK_2|$ has negative real part. Differentiating Eq. (D.1) two times w.r.t time, we get

$$\ddot{\sigma}(x) = K_1\ddot{x}(t) - \left[(K_1A - K_1BK_2)\,\dot{x}(t)\right] \tag{D.2}$$

For SOSMC, defining a new sliding surface as

$$\dot{\sigma}_n = \ddot{\sigma} + \gamma\dot{\sigma} \tag{D.3}$$

Solving Eqs. (D.2) and (D.3), we get

$$\dot{\sigma}_n = K_1\ddot{x}(t) - \left[(K_1A - K_1BK_2)\,\dot{x}(t)\right] + \gamma\dot{\sigma} \tag{D.4}$$

Simplifying Eq. (D.4) using Eq. (B.1), we get

$$\dot{\sigma}_n = K_1\left[A\dot{x}(t) + B\dot{u}(t) + \dot{\xi}(t)\right] - \left[(K_1A - K_1BK_2)\,\dot{x}(t)\right] + \gamma\dot{\sigma} \tag{D.5}$$

Defining the constant reaching law as

$$\dot{\sigma}_n = -\lambda\,\mathrm{sgn}(\sigma_n) \tag{D.6}$$

Solving Eqs. (D.5) and (D.6), we get

$$\begin{aligned} &-\lambda\,\mathrm{sgn}(\sigma_n) = K_1A\dot{x}(t) + K_1B\dot{u}(t) + K_1\dot{\xi}(t) \\ &-K_1A\dot{x}(t) + K_1BK_2\dot{x}(t) + \gamma\dot{\sigma} \\ \Rightarrow\ &-\lambda\,\mathrm{sgn}(\sigma_n) = K_1B\dot{u}(t) + K_1\dot{\xi}(t) + K_1BK_2\dot{x}(t) + \gamma\dot{\sigma} \\ \Rightarrow\ &\dot{u}(t) = -K_2\dot{x}(t) - (K_1B)^{-1}\left[\lambda\,\mathrm{sgn}(\sigma_n) + \gamma\dot{\sigma} + \|K_1\|\,\dot{\xi}(t)\right] \end{aligned} \tag{D.7}$$

To design the switching gain of Eq. (D.7), an adaptive tuning law is defined as given in Eq. (D.8). Finally, the control effort of SOSMC is obtained as described in Eq. (D.9).

$$\dot{\hat{\eta}} = \Gamma\,\|\sigma_n\| \qquad \text{for any } \Gamma > 0 \tag{D.8}$$

$$\dot{u}(t) = -K_2\dot{x}(t) - (K_1B)^{-1}\left[\hat{\eta}\,\mathrm{sgn}(\sigma_n) + \gamma\dot{\sigma} + \|K_1\|\,\dot{\xi}(t)\right] \tag{D.9}$$

Γ is the adaption gain.

Stability Proof :

Let the Lyapunov candidate be

$$V_4(\sigma_n, \tilde{\eta}) = \frac{1}{2}{\sigma_n}^T\sigma_n + \frac{1}{2}\tilde{\eta}^T\tilde{\eta} \tag{D.10}$$

where $\tilde{\eta} = \eta - \hat{\eta}$ and $\dot{\tilde{\eta}} = \left(\dot{\eta} - \dot{\hat{\eta}}\right) = -\dot{\hat{\eta}}$. Differentiating Eq. (D.10) w.r.t time, we get

$$\dot{V}_4 = {\sigma_n}^T\dot{\sigma}_n + \tilde{\eta}^T\dot{\tilde{\eta}} \tag{D.11}$$

Using Eq. (D.5), Eq. (D.11) is simplified as

$$\begin{aligned} &\dot{V}_4 = {\sigma_n}^T\Big(K_1\left[A\dot{x}(t) + B\dot{u}(t) + \dot{\xi}(t)\right] \\ &\quad -\left[(K_1A - K_1BK_2)\,\dot{x}(t)\right] + \gamma\dot{\sigma}\Big) - \tilde{\eta}^T\dot{\hat{\eta}} \\ \Rightarrow\ &\dot{V}_4 = {\sigma_n}^T\Big(K_1A\dot{x}(t) + K_1B\dot{u}(t) + K_1\dot{\xi}(t) \\ &\quad -K_1A\dot{x}(t) + K_1BK_2\dot{x}(t) - \gamma\dot{\sigma}\Big) - \tilde{\eta}^T\dot{\hat{\eta}} \\ \Rightarrow\ &\dot{V}_4 = {\sigma_n}^T\left(K_1B\dot{u}(t) + K_1\dot{\xi}(t) + K_1BK_2\dot{x}(t) - \gamma\dot{\sigma}\right) - \tilde{\eta}^T\dot{\hat{\eta}} \end{aligned} \tag{D.12}$$

Substituting $\dot{u}(t)$ from Eq. (D.9) into Eq. (D.12), we get

$$\dot{V}_4 = {\sigma_n}^T \left(K_1 B \left(-K_2 \dot{x}(t) - (K_1 B)^{-1} \begin{bmatrix} \hat{\eta}\ \mathrm{sgn}(\sigma_n) + \gamma \dot{\sigma} \\ + \|K_1\| \dot{\xi}(t) \end{bmatrix} \right) + K_1 \dot{\xi}(t) + K_1 B K_2 \dot{x}(t) - \gamma \dot{\sigma} \right) - \tilde{\eta}^T \dot{\hat{\eta}}$$

$$\Rightarrow \dot{V}_4 = {\sigma_n}^T \left(-K_1 B K_2 \dot{x}(t) - \hat{\eta}\mathrm{sgn}(\sigma_n) - \gamma \dot{\sigma} - \|K_1\| \dot{\xi}(t) + \|K_1\| \dot{\xi}(t) + K_1 B K_2 \dot{x}(t) - \gamma \dot{\sigma} \right) - \tilde{\eta}^T \dot{\hat{\eta}}$$

$$\Rightarrow \dot{V}_4 = {\sigma_n}^T \left(-\hat{\eta}\ \mathrm{sgn}(\sigma_n) \right) - \tilde{\eta}^T \dot{\hat{\eta}} \tag{D.13}$$

Using Eq. (D.8), Eq. (D.13) is further simplified as

$$\dot{V}_4 = {\sigma_n}^T \left(-\hat{\eta}\mathrm{sgn}(\sigma_n) \right) - \left(\eta - \hat{\eta} \right)^T \Gamma \|\sigma_n\| \tag{D.14}$$

Since ${\sigma_n}^T \mathrm{sgn}(\sigma_n) = \|\sigma_n\|$, Eq. (D.14) can be re-written as

$$\dot{V}_4 \leq -\hat{\eta} \|\sigma_n\|^2 - \left(\eta - \hat{\eta} \right)^T \Gamma \|\sigma_n\| \tag{D.15}$$

From Eq. (D.15), it is seen that $\dot{V}_4 < 0$, i.e., strictly negative definite. Therefore, invoking the Lyapunov direct method, it may be concluded that the designed sliding surface for the SOSMC is asymptotically stable.

Appendix E. Closed-loop stability analysis of MagLev system

Let the Lyapunov candidate be

$$V(x) = \frac{1}{2}\sigma^2 \tag{E.1}$$

Differentiating Eq. (E.1) w.r.t time, we get

$$\dot{V}(x) = \sigma \dot{\sigma} \tag{E.2}$$

Solving Eq. (44) and Eq. (E.2), we get

$$\dot{V}(x) = \sigma \left[\kappa_1 \dot{\varepsilon}_3 + \kappa_2 D^\alpha \varepsilon_3 \right] \tag{E.3}$$

Substituting Eqs. (41) and (45) into Eq. (E.3), we get

$$\dot{V}(x) = \sigma \left[\kappa_1 \left(-a_0 x_3 + b_0 u + d_2 \right) + \kappa_2 D^\alpha \varepsilon_3 \right]$$

$$\Rightarrow \dot{V}(x) = \sigma \left[-\kappa_1 a_0 x_3 - (\kappa_1 b_0)(\kappa_1 b_0)^{-1} \times \left\{ -\kappa_1 a_0 x_3 + \hat{\eta} + \kappa_2 D^\alpha \varepsilon_3 + \kappa_3 \sigma(t) + \kappa_4 \mathrm{sgn}(\sigma(t)) \right\} + \kappa_1 d_2 + \kappa_2 D^\alpha \varepsilon_3 \right]$$

$$\Rightarrow \dot{V}(x) = \sigma \left[-\kappa_1 a_0 x_3 + \kappa_1 a_0 x_3 - \hat{\eta} - \kappa_2 D^\alpha \varepsilon_3 - \kappa_3 \sigma(t) - \kappa_4 \mathrm{sgn}(\sigma(t)) + \kappa_1 d_2 + \kappa_2 D^\alpha \varepsilon_3 \right]$$

$$\Rightarrow \dot{V}(x) = -\sigma \left[\left(\hat{\eta} - \kappa_1 d_2 \right) + \left(\kappa_3 \sigma(t) + \kappa_4 \mathrm{sgn}(\sigma(t)) \right) \right] \tag{E.4}$$

Since $\sigma > 0$ and $\hat{\eta} > \kappa_1 d_2$, hence $\dot{V}(x) < 0$. Thus, invoking Lyapunov argument, it may be concluded that the closed-loop system with the designed controller is asymptotically stable.

References

[1] Tah A, Das D. Operation of small hybrid autonomous power generation systemin isolated, interconnected and grid connected modes. Sustain Energy Technol Assess 2016;17:11–25.

[2] Gampa SR, Das D. Real power and frequency control of a small isolated power system. Int J Electr Power Energy Syst 2015;64:221–32.

[3] Guha D, Roy PK, Banerjee S. Load frequency control of interconnected power system using grey wolf optimization. Swarm Evolut Comput 2016;27:97–115.

[4] Rout UK, Sahu RK, Panda S. Design and analysis of differential evolution algorithm based automatic generation control for interconnected power system. Ain Shams Eng J 2013;4(3):409–21.

[5] Hasanien HM. Whale optimisation algorithm for automatic generation control of interconnected modern power systems including renewable energy sources. IET Gener Transm Distrib 2018;12(3):607–14.

[6] Dhillon SS, Lather JS, Marwaha S. Multi objective load frequency control using hybrid bacterial foragingand particle swarm optimized PI controller. Electr Power Energy Syst 2016;79:196–209.

[7] Latif A, Hussain SMS, Das DC, Ustun TS. Double stage controller optimization for load frequency stabilization in hybrid wind-ocean wave energy based maritime microgrid system. Appl Energy 2021;282:116171.

[8] Dash P, Saikia LC, Sinha L. Comparison of performances of several cuckoo search algorithm based 2DOF controllers in AGC of multi-area thermal system. Electr Power Energy Syst 2014;55:429–36.

[9] Rahman A, Saikia LC, Sinha N. Load frequency control of a hydro-thermal system under deregulated environment using biogeography-based optimised three degree-of-freedom integral-derivative controller. IET Gener Transm Distrib 2015;9(15):2284–93.

[10] Guha D, Roy PK, Banerjee S. Optimal tuning of 3 degree-of-freedom proportional–integral–derivative controller for hybrid distributed power system using dragonfly algorithm. Comput Electr Eng 2018;72:137–53.

[11] Arya Y, Kumar N, Dahiya P, Sharma G, Celik E, Dhundhara S, Sharma M. Cascade-$I^\lambda D^\mu N$ controller design for AGC of thermal and hydrothermal power systems integrated with renewable energy sources. IET Renew Power Gener 2021;15(3):504–20.

[12] Dash P, Saikia LC, Sinha L. Flower pollination algorithm optimized PI-PD cascade controller in automatic generation control of a multi-area power system. Electr Power Energy Syst 2016;82:19–28.

[13] Baleanu D, Fernandez A, Akgü A. On a fractional operator combining proportional and classical differintegrals. Mathematics 2020;8(3):360.

[14] Guha D, Roy PK, Banerjee S. Performance evolution of different controllers for frequency regulation of a hybrid energy power system employing chaotic crow search algorithm. ISA Trans 2022;120:128–46.

[15] Khooban MH, Niknam T, Shasadeghi M, Dragicevic T, Blaabjerg F. Load frequency control in microgrids based on a stochastic non-integer controller. IEEE Trans Sustain Energy 2018;9(2):853–61.

[16] Arya Y. Effect of electric vehicles on load frequency control in interconnected thermal and hydrothermal power systems utilising CFFOIDF controller. IET Gener Transm Distrib 2020;14(14):2666–75.

[17] Debnath MK, Jena T, Sanyal SK. Frequency control analysis with PID-fuzzy-PID hybrid controller tuned by modified GWO technique. Int Trans Electr Energy Syst 2019;29(10):e12074.

[18] Sabanovic A. Variable structure systems with sliding modes in motion control-a survey. IEEE Trans Ind Inform 2011;7(2):212–23.

[19] Chen M, Shao S, Shi P. Robust adaptive control for fractional-order systems with disturbance and saturation. 1st ed.. Hoboken, NJ 07030, USA: Wiley; 2017.

[20] Gomaa Haroun AH, Li Yin-Ya. Ant lion optimized hybrid intelligent PID-based sliding mode controller for frequency regulation of interconnected multi-area power systems. Trans Inst Meas Control 2020;42(9):1594–617.

[21] Guha D, Roy PK, Banerjee S. Observer-aided resilient hybrid fractional-order controller for frequency regulation of hybrid power system. Int Trans Electr Energ Syst 2021;31(9):e13014.

[22] Do TD. Disturbance observer-based fuzzy SMC of WECSs without wind speed measurement. IEEE Access 2017;5:147–55.

[23] Esfahani Z, Roohi M, Gheisarnejad M, Dragicevic T, Khooban MH. Optimal non-integer sliding mode control for frequency regulation in stand-alone modern power grids. Appl Sci 2019;9(16):3411.

[24] Huang S, Xiong L, Wang J, et al. Fixed-time fractional-order sliding mode controller for multimachine power systems. IEEE Trans Power Syst 2021;36(4):2866–76.

[25] Bagheri A, Jabbari A, Mobayen S. An intelligent ABC-based terminal sliding mode controller for load-frequency control of islanded micro-grids. Sustainable Cities Soc 2021;64:102544.

[26] Sarkar MK, Dev A, Asthana P, Narzary D. Chattering free robust adaptive integral higher order sliding mode control for load frequency problems in multi-area power systems. IET Control Theory Appl 2018;12(9):1216–27.

[27] Wang J, Shaoa C, Chen YQ. Fractional order sliding mode control via disturbance observer for a class of fractional order systems with unmatched disturbance. Mechatronics 2018;53:8–19.

[28] Mi Y, Fu Y, Li D, Wang C, Loh PC, Wang P. The sliding mode load frequency control for hybrid power system based on disturbance observer. Electr Power Energy Syst 2016;74:446–52.

[29] Patel V, Guha D, Purwar S. Frequency regulation of hybrid power system using reduced order disturbance observer-based integral sliding mode controller. In: Proc. of 21st national power systems conference (NPSC). 2020, http://dx.doi.org/10.1109/NPSC49263.2020.9331888.
[30] Yang F, Muyeen SM, Li D, Lin S. Disturbance observer based fractional-order integral sliding mode frequency control strategy for interconnected power system. IEEE Trans Power Syst 2021;36(6):5922–32.
[31] Zhanga BT, Pi YG, Luo Y. Fractional order sliding-mode control based on parameters auto-tuning for velocity control of permanent magnet synchronous motor. ISA Trans 2012;51(5):649–56.
[32] Fei J, Lu C. Adaptive fractional order sliding mode controller with neural estimator. J Franklin Inst B 2018;355(5):2369–91.
[33] Pashaei S, Badamchizadeh M. A new fractional-order sliding mode controller via a nonlinear disturbance observer for a class of dynamical systems with mismatched disturbances. ISA Trans 2016;63:39–48.
[34] Zhou X, Li X. Trajectory tracking control for electro-optical tracking system based on fractional-order sliding mode controller with super-twisting extended state observer. ISA Trans 2021;117:85–95.
[35] Gurumurthy G, Das DK. Terminal sliding mode disturbance observer based adaptive super twisting sliding mode controller design for a class of nonlinear systems. Eur J Control 2021;57:232–41.
[36] Rashad R, El-Badawy A, Aboudonia A. Sliding mode disturbance observer-based control of a twin rotor MIMO system. ISA Trans 2017;69:166–74.
[37] Zeng X, Wang J, Wang X, Wang T. Design of sliding mode controller based on smdo and its application to missile control. Acta Aeronaut Astronaut Sin 2011;35(5):873–80.
[38] Yu-Sheng Lu. Sliding mode disturbance observer with switching-gain adaption and its application to optical disk drives. IEEE Trans Ind Electron 2009;56(9):3743–50.
[39] Yu D, Zhang W, Li J, Yang W, Xu D. Disturbance observer-based prescribed performance fault-tolerant control for a multi-area interconnected power system with a hybrid energy storage system. Energies 2020;13:1251.
[40] Adil HMM, Ahmed S, Ahmad I. Control of MagLev system using super-twisting and integral backstepping sliding mode algorithm. IEEE Access 2020;8:51352–62.
[41] Guo J. Application of full order sliding mode control based on different areas power system with load frequency control. ISA Trans 2019;92:23–34.
[42] Chen Y, Tang C, Roohi M. Design of a model-free adaptive sliding mode control to synchronize chaotic fractional-order systems with input saturation: An application in secure communications. J Franklin Inst B 2021;358:8109–37.
[43] Mousavi Y, Zarei A, Jahromi ZS. Robust adaptive fractional-order nonsingular terminal sliding mode stabilization of three-axis gimbal platforms. ISA Trans 2021. http://dx.doi.org/10.1016/j.isatra.2021.05.027.
[44] Prasad S, Ansari MR. Frequency regulation using neural network observer based controller in power system. Control Eng Pract 2020;102:104571.
[45] Arya Y. A new optimized fuzzy FOPI-FOPD controller for automatic generation control of electric power systems. J Franklin Inst B 2019;356(11):5611–29.
[46] Arya Y. Improvement in automatic generation control of two-area electric power systems via a new fuzzy aided optimal PIDN-FOI controller. ISA Trans 2018;80:475–90.
[47] Kumari S, Shankar G. Novel application of integral-tilt-derivative controller for performance evaluation of load frequency control of interconnected power system. IET Gener Trans Distrib 2018;12(14):3550–60.
[48] Guha D, Roy PK, Banerjee S. Disturbance observer aided optimised fractional-order three-degree-of-freedom tilt-integral-derivative controller for load frequency control of power systems. IET Gener Trans Distrib 2021;15:716–36.
[49] Akhmatov V. Analysis of dynamic behavior of electric power systems with large amount of wind power (Ph.D. dissertation), Lyngby: Technical Univ Denmark; 2003.
[50] Roy P, Roy BK. Sliding mode control versus fractional-order sliding mode control: Applied to a magnetic levitation system. J Control Autom Electr Syst 2020;31:597–606.
[51] Mane H, Wanaskar V, Chaudhari S, et al. Novel two time scale observer based sliding mode control with velocity estimator for magnetic levitation. In: Proc of 2021 int conf on smart generation computing, communication and networking (SMART GENCON). 2021, p. 1–6. http://dx.doi.org/10.1109/SMARTGENCON51891.2021.9645849.
[52] Ginoya D, Gutte CM, Shendge PD, Phadke SB. State-and-disturbance-observer-based sliding mode control of magnetic levitation systems. Trans Inst Meas Control 2016;38(6):751–63.
[53] Bevrani H. Robust power system frequency control. 2nd ed.. Springer; 2014.
[54] Prasad S, Purwar S, Kishor N. Non-linear sliding mode load frequency control in multi-area power system. Control Eng Pract 2017;61:81–92.